UNIVERSITY OF CALGARY

Engineering Atomic and Optical Quantum States using Four-Wave Mixing

by

John Travis Brannan

A THESIS
SUBMITTED TO THE FACULTY OF GRADUATE STUDIES
IN PARTIAL FULFILLMENT OF THE REQUIREMENTS FOR THE
DEGREE OF MASTER OF SCIENCE

DEPARTMENT OF PHYSICS AND ASTRONOMY

CALGARY, ALBERTA
MAY, 2014

Abstract

This thesis presents a study of the four-wave mixing process in hot Rubidium vapor and its applicability to generating arbitrary quantum states, both in the optical domain and as atomic collective spin excitations. The four-wave mixing process involves a double Raman scattering event, where conservation of energy and momentum entangle these Raman-scattered photons. Heralding upon detection of one of these photons in a given mode projects the other photon onto a single photon Fock state in a well-defined mode, which may serve as a narrowband quantum light source that is compatible with atom-based quantum communication protocols.

We integrate the existing technique of conditional measurements into our detection scheme, which allows us to engineer more complex quantum states. Experimentally we demonstrate the production of arbitrary superpositions of $|0\rangle$ and $|1\rangle$ in the optical Fock basis. We also present a theoretical model of this process which incorporates experimental complications such as losses, higher photon-number states, and a non-trivial temporal mode. This scheme can be extended to generate arbitrary quantum states with increasing photon numbers, at the expense of repetition rate.

The atomic nature of this four-wave mixing process has an added benefit in that it allows access to excitations of the collective atomic ensemble. The optical results demonstrate the creation of transient collective spin excitations, and we present a proposal to extend this work to generate longer lived arbitrary collective atomic states.

Acknowledgements

After many days in isolation trying to finish writing this thesis, powered by caffeine and fast food, one might think that doing a Master's is a lonely job. However, in reality this is not true at all. I owe a great deal to the many people who have been there and supported me throughout this process.

First and foremost, I should thank my supervisor Alex Lvovsky. When I joined his group as an undergraduate summer student five years ago, it was my first taste of what experimental research entailed and I enjoyed it greatly. So much so, that after spending three years completing my undergrad and trying out other research fields in physics, I decided I wanted more and came back for a Master's project. I thank him for not only his patience and financial support, but also for teaching me a good chunk of what I know in this field. I have found that his solutions to problems, which I was often skeptical of and were not usually immediately clear to me, were almost always right. One thing that I will take away from this experience is to always ask the question that Alex often posed to us during our many reader's clubs: "What is the physics?"

I would also like to thank the many amazing group members that I have worked with over the years here. In particular I have learned a great many things from Andrew MacRae, who was the PhD student working on this project when I joined and is now doing a Postdoc at UC Berkeley. His understanding of the technical details involved always impressed me, and much of my own understanding came from trying to absorb his knowledge and experience as I worked with him. His friendship and attitude in the lab made working on this a much more enjoyable experience.

I would also like Zhongzhong Qin and Adarsh Shankar Prasad who have joined in on working on this project. There was a point where progress had stalled due to equipment issues and I began to lose my motivation, however their curiosity and diligence has helped

motivate me to push though any difficulties that we encounter. I am grateful not only for their contributions to the project but also for their friendship and helping to keep me sane through all of this. I would also like to thank my coworkers who were always there for interesting conversations and made life in the group more enjoyable throughout my time here. Alphabetically, these are Aleksey, Andal, Anna, Arina, Arturo, Aveek, Boris, Chris, Connor, Daniel, Di, Eden, Erick, Eugene, Geoff, Pan, Ranjeet, Ryan, Tayebe, and Yuri.

Finally, I would like to thank my parents, and my friends and family outside of the University. Their continuous support and encouragement has helped me to get through the stressful times, and I don't think I would have made it without them.

Table of Contents

List of Figures and Illustrations

Publications Arising from this Work

A MacRae, T Brannan, R Achal, and AI Lvovsky. Tomography of a high-purity narrowband photon from a transient atomic collective excitation. *Physical Review Letters,* 109(3):033601, 2012. [1]

T Brannan, Z Qin, A MacRae, and AI Lvovsky. Generation and tomography of arbitrary qubit states in a transient collective atomic excitation. *arXiv:1403.3463* [2]

List of Symbols, Abbreviations and Nomenclature

Symbol	Definition
AOM	Acousto-optic modulator
APD	Avalanche photodiode
BHD	Balanced homodyne detection
BS	Beamsplitter
CSE	Collective spin excitation
DLCZ protocol	Duan Lukin Cirac Zoller protocol
ECDL	External cavity diode laser
EOM	Electro-optic modulator
FWM	Four-wave mixing
FWHM	Full width at half maximum
HD	Homodyne detector
LO	Local oscillator
PBS	Polarizing beamsplitter
POVM	Positive-valued operator measure
QSHO	Quantum simple harmonic oscillator
SPCM	Single photon counting module
SPDC	Spontaneous parametric down-conversion
TMSS	Two-mode squeezed state
TMSV	Two-mode squeezed vacuum

Chapter 1

Introduction

In this thesis, I will describe an experiment which investigates the use of a four-wave mixing (FWM) process in hot Rubidium vapor to generate nonclassical states in both light and matter. A more detailed description of what it means to be nonclassical can be found in Chapter 2, but the core concept of nonclassicality is any state which can't be described by classical mechanics. The acts of storing, measuring, and transmitting this nonclassical information are at the center of experimental quantum information science. The natural candidate for transmission of this quantum information is the photon, driven by its ability to travel at the speed of light and its tendency to interact with the environment only very weakly [3]. As a result, a number of important quantum effects have been reformulated and demonstrated in the optical domain. A test of the famous EPR paradox proposed by Einstein, Podolsky and Rosen [4] was proposed by Bell [5] and then reformulated optically in the more experimentally convenient CHSH inequality [6], which was later demonstrated experimentally [7]. The interference between indistinguishable photons led to quantum interference effects such as the Hong Ou Mandel effect [8]. Hanbury Brown and Twiss's experiment on photon-antibunching initiated the concept of characterizing a state from the counting photons and inferring the photon number statistics [9]. All in all, photons have been fertile ground for quantum physics over the last century, and likely will stay that way well into the next century.

The applications of nonclassical states are quite diverse, and in recent years there has been significant progress to developing quantum optical technologies using these states. One of the most significant of these is the development of quantum cryptography, which promises unconditionally secure communications [10] by generating a shared key over a quantum

channel. These quantum key distribution protocols are in practice limited in the distance that they can function due to optical losses and equipment limitations, and as such there is considerable interest in the development of quantum repeaters that would allow for the extension of this distance [11, 12]. These protocols typically use qubits, the quantum analogue of a binary classical bit as the carrier of information and as such, to implement these systems requires a reliable and efficient method for the creation and measurement of these qubits.

Squeezed states have also garnered considerable interest for their application to precision measurements. They have been applied to the development of increasingly sensitive time standards [13] and to enhanced sensitivity for ultra-precise interferometers used as gravitational wave detectors [14], among other metrology applications [15]. Entangled states such as Bell states and two-mode squeezed states have found applications in quantum teleportation [16], long distance entanglement distribution [17], quantum networks [18], and quantum computation [19]. All of these require the generation and measurement of certain nonclassical states, and ultimately we strive towards complete control over the Hilbert space of the states that are used. For a single mode state, this can be achieved using projective measurements, akin to the procedure demonstrated by Bimbard *et al.* [20]. Use of this technique has shown the generation of an arbitrary optical superposition state up to $n = 2$ in the Fock basis, and in principle this can be extended to higher photon numbers at the expense of decreased generation rate.

While optical systems are ideal for the communication of information, the storage of information on photons is not ideal as they tend not to stay in one place. For this purpose, many other systems are strong candidates, including collective atomic systems, superconducting circuits, trapped ions, and quantum dots. However, the manipulation and engineering of quantum states in these systems is not as widely developed as it is for light, and the usable techniques vary from system to system. Some examples of quantum state engineering in

these systems include: superconducting circuits [21], trapped ion ensembles [22], and quantum dots [23]. Collective atomic systems are much more difficult to manipulate directly, as the excitation is distributed across all of the atoms and it is not easy to directly access. In this thesis, we describe a method for manipulating the state of a collective atomic excitation indirectly, by generating entanglement between the collective atomic state and an optical state, then performing projective measurements on the optical state. Engineering arbitrary quantum states of these collective atomic excitations can find applications in quantum memories [24], quantum repeaters [11], quantum logic gates [25], and quantum metrology [26].

The standard method for generating nonclassical light is a nonlinear optical process known as spontaneous parametric down-conversion (SPDC). In this process, a single high-frequency photon is efficiently converted to two low-frequency photons, where conservation of energy and momentum entangles these photons together [27]. These photons are always generated in pairs, and the output can be shown to be a two-mode squeezed state. By heralding upon the measurement of a single photon in one of these modes, the other mode is projected onto a single photon Fock state, thus making this a practical source of single photons as well [28]. One drawback to this technique is the large bandwidth of the output photons, which can be dealt with by filtering down to a suitable bandwidth at the cost of greatly reducing the rate of usable photon pair events [29]. Another approach is to place the SPDC process in an optical cavity [30, 31].

An alternative method for generating nonclassical light is a third-order nonlinear effect known as four-wave mixing (FWM). In this process, two input photons are absorbed and then a pair of entangled output photons are emitted. Similar to SPDC, this creates a two-mode squeezed state that can be made into a single photon source, which is the approach taken in this work. The first demonstration of squeezed light was generated this way [32]. More recently, the DLCZ protocol [11] has led to the development on an on-demand photon source [33, 34, 35] from atomic excitations. By placing the ensemble of atoms in a high

finesse cavity, a photon source with very narrow bandwidth and high brightness has been demonstrated [36]. Recently, the efficient generation of squeezed light has been demonstrated at levels comparable to SPDC [37]. One of the advantages of FWM is that it has a much narrower bandwidth than SPDC, leading to a high ratio of generated events to signal bandwidth, which is known as *spectral brightness* [38]. Our own previous work has shown high efficiency generation of single photons comparable to SPDC, while maintaining a high spectral brightness [1].

Another major appeal of this FWM process is that it allows for manipulation and measurement of the collective atomic state. By following along the lines of the DLCZ protocol, the two Raman scattering events involved in FWM can be time separated. After the first Raman scattering, the excitation of the collective atomic state is entangled with the Raman-scattered photon. Conditional measurements can be performed on this photon, projecting the atomic state onto an arbitrary, controllable superposition state. This state can then be read out optically via the second Raman scattering event, returning the atoms to their original state.

The purpose of this thesis is to demonstrate the generation of arbitrary optical qubits from an atomic FWM source. We aim to show that FWM is competitive with SPDC and investigate the effects of losses in our system. We characterize the qubit using homodyne tomography. Determination of the signal temporal mode is important for efficient state reconstruction, and we descibe advancements for experimental determination of this temporal mode. Furthermore, we describe the potential extension of our experiment into a DLCZ scheme, allowing for the creation of arbitrary collective atomic excitations.

This thesis is organized as follows. Chapter 2 provides some background information about nonclassical states and how we can define and classify them. A description of the various methods of experimentally detecting and classifying quantum states of light is also given. Chapter 3 describes the four-wave mixing process used in this experiment and its

application to generating nonclassical states of light. Experimental results and a characterization of our system as a nonclassical light source are given. Chapter 4 describes the quantum state engineering technique, and experimental results for generating arbitrary optical qubits are shown. A theoretical model incorporating experimental imperfections is presented and applied to the experimental data, and a promising avenue for overcoming one of these experimental limitations is discussed. Chapter 5 describes an extension of this work to atomic state engineering, and presents our progress towards this goal. Chapter 6 presents a summary of our work, along with an outlook for the future steps in this project.

Chapter 2

Quantum States

2.1 Quantum Light

Over the course of history, light has been thought of in many ways. The classical description of light considers it as a wave, which acts as a solution to Maxwell's equations for a particular geometry. However this description turned out to incomplete and could not account for the results of experiments such as the Planck distribution for black-body radiation [39], or the Compton effect [40]. These phenomena required the quantization of the electromagnetic field to explain, and in this way the idea that light is made up of quantized photons was developed. Interestingly, one of the experiments at the forefront of the development of a quantum mechanical description of light was the photoelectric effect, which can actually be explained using a classical electromagnetic field description with quantization of atoms and electrons [41].

Classical electromagnetism tells us that the solutions to Maxwell's equations in free space can be broken up into spatio-temporal modes $u(\vec{x}, t)$, which collectively give a complete description of the field. The simplest of these modes are plane waves, which for some polarization have $u(\vec{x}, t) = e^{i(\vec{k}\cdot\vec{x}-\omega t)}$ [42]. These plane waves form the Fourier components of the electromagnetic field, and thus more complex modes can be written as a sum of these plane wave modes. A quantum mechanical description of the electromagnetic field tells us that each of these modes behaves as a quantum simple harmonic oscillator (QSHO). We associate an annihilation operator $\hat{a}$ to a given mode, and then the Hamiltonian for that mode in terms of $\hat{a}$ becomes:

$$\hat{H} = \hbar\omega\left(\hat{a}^\dagger\hat{a} + \frac{1}{2}\right) \tag{2.1}$$

Given that the properties of the QSHO are well-known, we can use it to characterize the

quantum state of one of these spatio-temporal modes.

Following the basic theory of quantum mechanics, we define quadrature operators from the creation and annihilation operators:

$$\hat{X} = \frac{\hat{a}^\dagger + \hat{a}}{\sqrt{2}} \tag{2.2}$$

$$\hat{P} = i\frac{\hat{a}^\dagger - \hat{a}}{\sqrt{2}} \tag{2.3}$$

We can rewrite the Hamiltonian in terms of these quadrature operators, yielding the expression:

$$\hat{H} = \frac{1}{2}\hbar\omega\big(\hat{X}^2 + \hat{P}^2\big) \tag{2.4}$$

Despite the creation and annihilation operators having fundamental theoretical importance, the quadrature operators are particularly useful as they are Hermitian and thus can be physically measured. The eigenstates of these operators, while not normalizable, are mathematically convenient to use and are defined by: $\hat{X}|X\rangle = X|X\rangle$, $\hat{P}|P\rangle = P|P\rangle$. These eigenstates are related to each other following:

$$\langle X|X'\rangle = \delta(X - X') \tag{2.5}$$

$$\langle P|P'\rangle = \delta(P - P') \tag{2.6}$$

$$\langle X|P\rangle = \frac{1}{\sqrt{2\pi}}e^{iPX} \tag{2.7}$$

Using the canonical commutation relation $[\hat{a}, \hat{a}^\dagger] = 1$ we find that $[\hat{X}, \hat{P}] = i$ and thus the quadrature operators must obey the uncertainty relation [43]:

$$\langle \Delta X^2\rangle\langle \Delta P^2\rangle \geq \frac{1}{4} \tag{2.8}$$

We can also define the number operator as:

$$\hat{n} \equiv \hat{a}^\dagger\hat{a} \tag{2.9}$$

This number operator is another useful physical observable, corresponding to the number of photons in the field. The eigenstates of the number operator are known as *Fock states* and

are denoted by $|n\rangle$ for $n \geq 0$. The creation and annihilation operators act on the Fock states by adding or removing an excitation respectively from the electromagnetic field by:

$$\hat{a}^\dagger|n\rangle = \sqrt{n+1}|n+1\rangle \tag{2.10}$$

$$\hat{a}|n\rangle = \sqrt{n}|n-1\rangle \tag{2.11}$$

Starting from the vacuum state $|0\rangle$, we can construct any Fock state using the creation operator:

$$|n\rangle = \frac{(\hat{a}^\dagger)^n}{\sqrt{n!}}|0\rangle \tag{2.12}$$

From the Hamiltonian (2.1) we see that these Fock states correspond to energy eigenstates with eigenvalue $\hbar\omega(n+\frac{1}{2})$. The Fock states form an orthonormal basis

$$\langle m|n\rangle = \delta_{mn} \tag{2.13}$$

which is used as the canonical basis in which arbitrary quantum states are represented in this work.

Another useful description of a state is given by its wavefunction in the quadrature basis $\psi(X) = \langle X|\psi\rangle$. For Fock states this is given by:

$$\psi_n(X) = \frac{e^{-\frac{X^2}{2}}}{\pi^{1/4}\sqrt{2^n n!}} H_n(X) \tag{2.14}$$

where $H_n(X)$ is the Hermite polynomial of order n. In the event that there are no excitations of the field (called the *vacuum* state where $n = 0$), the wavefunction is given by the minimum-uncertainty Gaussian mode $\psi_0(X) = \frac{1}{\pi^{1/4}} e^{-\frac{X^2}{2}}$.

Although we have defined the Fock states as number eigenstates of a QSHO, they have properties that are very different from what one would expect for a classical harmonic oscillator. For example, the mean value of the quadratures of a Fock state is zero, as compared to the $\langle X(t)\rangle = X(0)\cos(\omega t) + P(0)\sin(\omega t)$ behavior that would expect for say, a classical pendulum. We expect though that the quantum description should be able to predict the

behavior of classical systems in the large quantum number limit, which does not hold at all for pure Fock states. From this, the need arises for a pseudo-classical state which behaves like a classical harmonic oscillator in the classical limit. This state, known as a *coherent state*, was initially discovered by Schrödinger [44] as he was searching for a quantum state with classical-like properties to satisfy the correspondence principle. More practically for this work, it described in terms of quantum optics by Glauber [45]. It is formally defined as an eigenstate of the annihilation operator:

$$\hat{a}|\alpha\rangle = \alpha|\alpha\rangle \tag{2.15}$$

Here, α describes the amplitude and phase of the state and is complex-valued in general. Note that $\alpha = 0$ is also valid, indicating that the vacuum state is also a coherent state with zero amplitude. The coherent state has several important properties which we take advantage of in this work. It is also the state of a laser output, which makes it easily obtainable in a lab setting [46].

We can express these coherent states in the Fock basis, where unlike the individual Fock states they do not have a definite photon number:

$$|\alpha\rangle = e^{-\frac{|\alpha|^2}{2}} \sum_{n=0}^{\infty} \frac{\alpha^n}{\sqrt{n!}} |n\rangle \tag{2.16}$$

Here the photon number probability follows a Poissonian distribution. The mean photon number of a coherent state can be calculated as:

$$\langle n \rangle_\alpha = \langle \alpha | \hat{a}^\dagger \hat{a} | \alpha \rangle = \alpha^* \alpha \langle \alpha | \alpha \rangle = |\alpha|^2 \tag{2.17}$$

and similarly, the photon number variance is:

$$\langle \Delta n^2 \rangle_\alpha = \langle n^2 \rangle_\alpha - \langle n \rangle_\alpha^2 = |\alpha|^2 \tag{2.18}$$

Note that coherent states are minimum uncertainty states satisfying the equality in Equation (2.8):

$$\langle \Delta \hat{X}^2 \rangle_\alpha = \frac{1}{2} \tag{2.19}$$

indicating that even coherent states with non-zero amplitude have the same quadrature variance as vacuum. In fact, one can write a coherent state in terms of the phase-space displacement operator as $|\alpha\rangle = \hat{D}(\alpha)|0\rangle$, with the displacement operator defined as:

$$\hat{D}(\alpha) = e^{\alpha\hat{a}^\dagger - \alpha^*\hat{a}} \tag{2.20}$$

We can determine the time evolution of these states using the evolution operator $e^{-i\hat{H}t/\hbar}$:

$$|\alpha(t)\rangle = e^{-i\hat{H}t/\hbar}|\alpha(0)\rangle = e^{-i\omega t/2}|e^{-i\omega t}\alpha(0)\rangle \tag{2.21}$$

Considering that $|e^{-i\omega t}\alpha(0)\rangle$ is also a coherent state with simply a different phase, we see that coherent states evolve by plotting a circular trajectory in phase-space. Thus, these coherent states follow a trajectory similar to a classical harmonic oscillator: $\langle X(t)\rangle = \langle X(0)\rangle \cos(\omega t) + \langle P(0)\rangle \sin(\omega t)$.

2.2 Density Matrix and Wigner Function

Up to this point, each quantum state that we have introduced has been representable by a single state vector $|\psi\rangle$. These are the so called *pure states*, which can be represented as quantum superpositions of the basis eigenvectors. However, there is another class of states known as *mixed states*, which are statistical mixtures of multiple pure states and thus cannot be represented using a single state vector. For these states, it is useful to introduce the density operator:

$$\hat{\rho} = \sum_i P_i |\psi_i\rangle\langle\psi_i| \tag{2.22}$$

where P_i is probability of the system being found in state $|\psi_i\rangle$. The density matrix has a few useful properties as expressed below:

$$\langle\hat{A}\rangle = \mathrm{Tr}[\hat{\rho}\hat{A}] \tag{2.23}$$

$$\mathrm{Tr}[\hat{\rho}] = 1 \tag{2.24}$$

Typically the Fock basis is chosen to represent density matrices, in which case we can expand out the elements as follows:

$$\rho_{mn} = \langle m|\hat{\rho}|n\rangle = \sum_i P_i \langle m|\psi_i\rangle\langle\psi_i|n\rangle \tag{2.25}$$

The definition of the density operator allows for the introduction of one the most experimentally relevant mixed states, which is known as the *thermal state*. This is the state that is produced by a randomly emitting, incoherent source of photons, such as a heated filament. This state requires a statistical mixture of photons to represent, and has a density matrix given by:

$$\hat{\rho} = \frac{1}{G}\sum_{n=0}^{\infty}\Big(\frac{G-1}{G}\Big)^n |n\rangle\langle n| \tag{2.26}$$

where $G \equiv \frac{1}{1-e^{-\beta}} = \bar{n}+1$, with $\beta = \frac{\hbar\omega}{k_B T}$ related to the thermal state temperature and $\bar{n}$ being the mean number of photons in the field. One can calculate the photon number variance $\langle\Delta n^2\rangle = \bar{n}^2 + \bar{n}$ and the quadrature variance $\langle\Delta X^2\rangle = \bar{n} + 1/2$.

Classically, one of the most useful ways to characterize the state of a system is to look at its trajectory in phase space. For an ensemble of identically prepared objects, one can define the classical phase space density function $W_c(X,P)$ from which the probability of finding the object in a region R of phase space is given by $P_R = \iint_R W_c(X,P)dXdP$. Since classically the phase space density function can be arbitrarily narrow, the definition of probability requires that the W_c is real and non-negative. In order to determine W_c, we can experimentally measure either of the coordinates X and P repeatedly and build up a statistical distribution of the results. These probability distributions $Pr(X)$ and $Pr(P)$, known as marginal or quadrature distributions, are related to the phase space density function by:

$$Pr(X) = \int_{-\infty}^{\infty} W_c(X,P)dP \tag{2.27}$$

$$Pr(P) = \int_{-\infty}^{\infty} W_c(X,P)dX \tag{2.28}$$

Quantum mechanically, we cannot define a phase space probability function in the same way, since this would require simultaneous determination of both X and P. We know these

do not commute and must follow the uncertainty relation (2.8). What we can do however, is measure a particular coordinate for an ensemble of identically prepared quantum states and then build up the marginal distributions. This could be X, P, or a generalized coordinate which can be any linear combination of the two:

$$\hat{X}_\theta \equiv \hat{X}\cos\theta + \hat{P}\sin\theta \tag{2.29}$$

Although it no longer has a meaning as a probability distribution, we can still define a phase-space function that satisfies the marginal relations (2.27, 2.28) in the quantum case. This function, called the *Wigner function* [47], is defined by:

$$W(X,P) = \frac{1}{2\pi}\int_{-\infty}^{\infty} e^{iPQ}\Big\langle X - \frac{Q}{2}\Big|\hat{\rho}\Big|X + \frac{Q}{2}\Big\rangle dQ \tag{2.30}$$

The Wigner function, although not a probability distribution, has many similarities to the classical probability distribution. They are both real and normalized: $\iint_{-\infty}^{\infty} W(X,P)dXdP = 1$. The marginal distribution for a general coordinate X_θ is obtained by projection onto the X_θ axis:

$$Pr(X_\theta) = \int_{-\infty}^{\infty} W(X_\theta, P_\theta)dP_\theta \tag{2.31}$$

The Wigner function is also linear with respect to the density matrix, so the Wigner function for a mixed state is the sum of the Wigner functions of the constituent pure states. It uniquely defines the state as well, since the density matrix in a given basis can be uniquely recovered from the Wigner function [42]:

$$\langle m|\hat{\rho}|n\rangle = 2\pi\iint_{-\infty}^{\infty} W_{\hat{\rho}}(X,P)W_{|m\rangle\langle n|}(X,P)dXdP \tag{2.32}$$

Contrasting to the classical probability distribution, the Wigner function can take negative values, and often does for states that can't be represented classically. By the nature of the marginal distributions representing probabilities though, each negative valley must necessarily be surrounded by a positive hill so that the marginals are non-negative. A few examples of Wigner functions for various states are shown in Figure 2.1, with the single photon Fock state demonstrating these nonclassical valleys of negativity.

For a given state in the Fock basis $\hat{\rho} = \sum_{m,n} \rho_{mn}|m\rangle\langle n|$, we can express the Wigner function in terms of the position wavefunctions:

$$W(X,P) = \sum_{m,n} \frac{1}{2\pi} \int_{-\infty}^{\infty} e^{iPQ} \psi_m^*(X - \frac{Q}{2}) \psi_n(X + \frac{Q}{2}) dQ \tag{2.33}$$

This form is often useful practically for quick computation of Wigner functions.

2.3 Nonclassicality

In the field of quantum optics, one looks at all sorts of quantum optical states, which can have very different properties and interactions. It is important to be able to classify and communicate the states that we are working with. In some sense, since quantum optics applies a quantum mechanical treatment to the electromagnetic field, all optical states are quantum states. However, some of these states have a classical analogue and thus are limited by the properties of classical mechanics, while other states do not. In this sense, all states which cannot be expressed classically are *nonclassical*. As we have seen, the coherent state has the properties of a classical harmonic oscillator, and we can use this to help classify classical states from nonclassical states. Any quantum state that can expressed as a statistical mixture of coherent states is defined as a *classical* state, while any quantum state that cannot be expressed this way is a *nonclassical* state. There are several different sufficient but not necessary nonclassicality criteria that can help to distinguish if a state is nonclassical or not, a few of which are explored below.

2.3.1 Squeezing Criteria

The coherent state is a minimum uncertainty state, where $\langle \Delta X_\theta^2 \rangle = 1/2$ for all θ so that the equality of (2.8) is satisfied. While the uncertainty relation (2.8) holds true for all quantum states, some states can have $\langle \Delta X_\theta^2 \rangle < 1/2$ for some values of θ and a corresponding increased variance along the orthogonal coordinate. These are known as *quadrature squeezed* states. To see that any state satisfying $\langle \Delta X_\theta^2 \rangle < 1/2$ for some θ is nonclassical, we can look at the

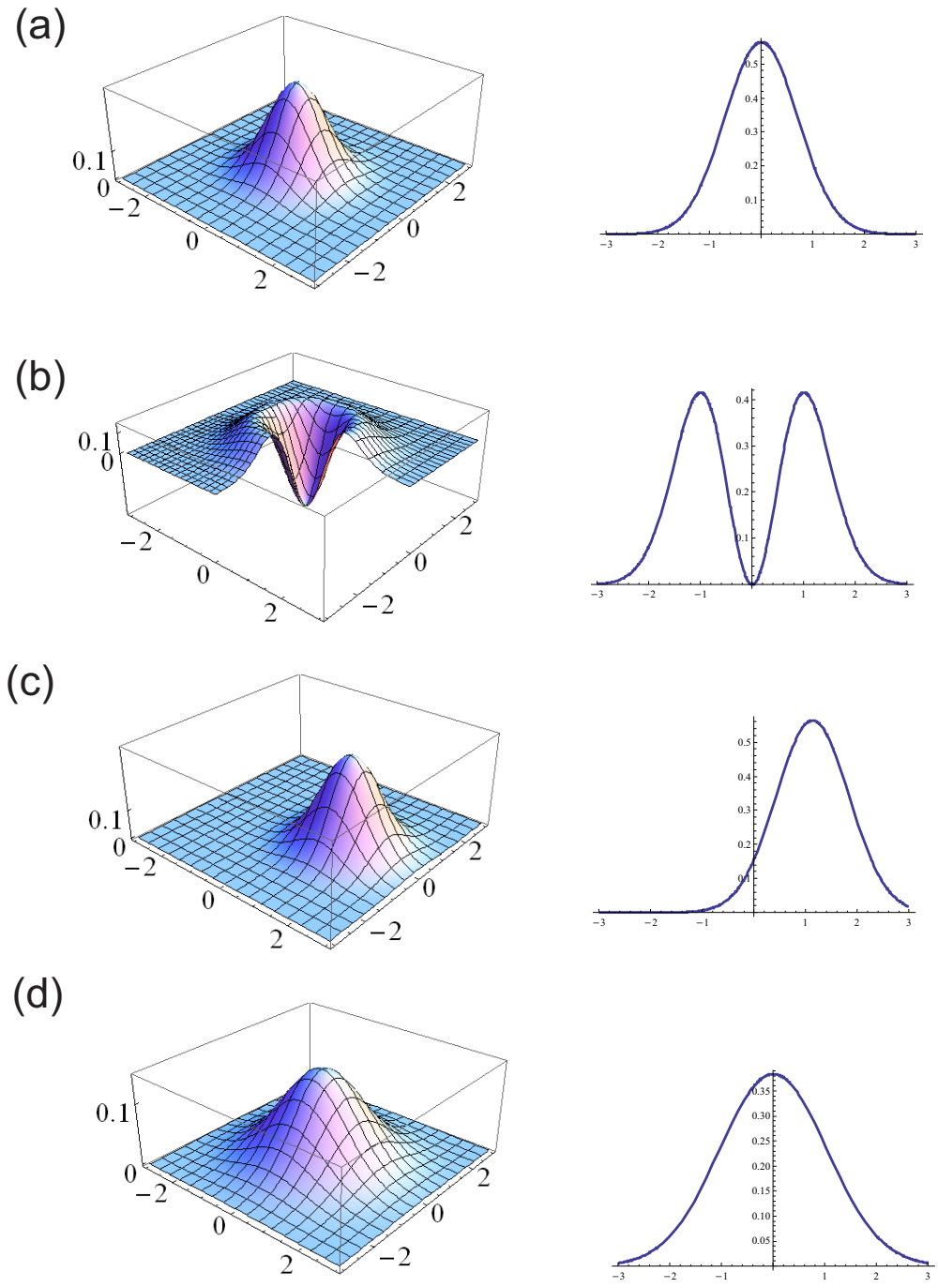

Figure 2.1: Wigner functions and corresponding marginal distributions for various states. (a) The vacuum state $|0\rangle$. (b) The single photon state $|1\rangle$. (c) A coherent state $|\alpha\rangle$ with $\alpha = 0.8$. (d) A thermal state with $\beta = 1$.

quadrature variance of a statistical mixture of coherent states. Each coherent state will have a Gaussian marginal distribution with variance $\langle \Delta X_\theta^2 \rangle = 1/2$. The marginal distribution of a statistical mixture of two coherent states will then simply be the weighted sum of the individual marginal distributions. Since the marginal distributions are necessarily non-negative, the resulting sum will have a variance $\langle \Delta X_\theta^2 \rangle \geq 1/2$ with the equality only arising if the marginal distributions are identical. Therefore, any state with $\langle \Delta X_\theta^2 \rangle < 1/2$ cannot be represented as a sum of coherent states and then is nonclassical.

2.3.2 Negativity of Wigner Function

The Wigner function of a coherent state is a Gaussian function that can be described as the displacement of the vacuum Wigner function in phase space by $\hat{D}(\alpha)$. Since the vacuum Wigner function is non-negative at all points in phase space and Wigner functions add linearly, the statistical mixture of multiple coherent states must necessarily also have a Wigner function which is non-negative at all points in phase space. Thus, any state which has a negative Wigner function cannot be expressed as a statistical mixture of coherent states and is a nonclassical state. For an example of this, any odd Fock state has a highly negative Wigner function at the origin $W_{\rho_{odd}}(0,0) = -\frac{1}{\pi}$.

2.3.3 Limits on ρ_{11}

For a given density matrix, we may wish to be able to tell if it is nonclassical simply by looking at some of its elements. Of particular relevance to this is the ρ_{11} density matrix element, as we later characterize an experimental single photon source. For a coherent state, (2.16) gives $\rho_{11} = e^{-|\alpha|^2}|\alpha|^2 = \bar{n}e^{-\bar{n}}$ since $\bar{n} = |\alpha|^2$. Taking $\frac{d}{d\bar{n}}\rho_{11} = (1-\bar{n})e^{-\bar{n}} = 0$, we find the maximum value for ρ_{11} occurs when $\bar{n} = 1$, and has a value of $\rho_{11} = e^{-1} \approx 0.37$. For a statistical mixture of coherent states, $\hat{\rho} = \sum_\alpha c_\alpha \rho_\alpha$, $\rho_{11} = \sum_\alpha c_\alpha \rho_{11,\alpha} \leq \max[\rho_{11}] \sum_\alpha c_\alpha = e^{-1}$. Therefore, all classical states have $\rho_{11} \leq e^{-1}$ and any state with $\rho_{11} > e^{-1}$ must be nonclassical.

2.4 Detection of Quantum Light

2.4.1 Intensity Detection

The typical way of detecting light is to take advantage of the photo-electric effect to convert a photon flux into a current of electrons, which is much easier to amplify and measure electronically. One of the most common detectors in optics is known as a photodiode, and uses just this effect in a semiconductor diode. Incident photons excite electron-hole pairs, which flow to separate ends of the diode in the presence of a bias electric field. This electric current can then be amplified and measured on an oscilloscope in the lab. The probability of an incident photon being converted to a photoelectron is known as the quantum efficiency η. For silicon PIN photodiodes in the near-IR band, quantum efficiencies of $\eta > 90\%$ are available.

One of the key parameters that we are often interested in measuring is the noise of the detected light. As mentioned earlier, typical states of light have some variance in photon number. Any classical state will have at least the variance of a coherent state, which is given by $\langle \Delta n^2 \rangle = |\alpha|^2$. This fundamental variance in the number of photons in the state causes a corresponding noise in the photocurrent known as *shot noise*, and it sets a limit on the minimum noise that can exist in a classical state. There can also be additional noise introduced on top of this of course, often due to amplitude and phase fluctuations in the light source or extra noise added in the amplification process. This noise is known as *technical noise* or classical noise, and is introduced by imperfections in the equipment. It is possible to distinguish these two types of noise using a 50:50 beamsplitter and two identical detectors. Taking subtraction of the signals from each detector will cancel any technical noise that exists in the beam leaving only the shot noise and electronic noise, while the sum of the signals will give the technical noise on top of the shot noise and electronic noise. Since the electronic noise can be measured by looking at the detector output with no input beam, all three of these noise sources can be separated and measured.

2.4.2 Single Photon Detection

Despite the relatively high quantum efficiency of photodiodes, sensitivity down to the single photon level is out of the range of any basic photodiode. Even for a diode with perfect quantum efficiency, one photon will only be converted to one photoelectron and a correspondingly minuscule current that is not detectable without amplification. Typical minimum power for a standard photodiode is on the scale of about 1nW, which for 795 nm light corresponds to approximately 10^9 photons per second. The current this 10^9 photoelectrons per second provides is still only on the order of 100 pA, which is near the limit of current electronics. 10^9 photons per second is quite far off from the single-photon resolution that we would ideally like for nonclassical light detection, and restricts its applicability to measuring nonclassical light states without some clever modifications of the equipment.

One of these clever modifications is taken advantage of in an avalanche photodiode (APD). An APD increases the bias voltage immensely, so that emitted photoelectrons will be accelerated to such high velocities that they will ionize other atoms upon impact, resulting in an avalanche of electrons and a huge gain. When the bias voltage is set above the breakdown voltage of the diode, a single photodetection will result in a huge, self-sustaining avalanche of electrons, allowing for detection of a single photon. This regime is called Geiger mode or trigger mode, as each single photon results in a huge trigger current with extremely quick time resolution (on the order of 100ps). After each detection event, the avalanche must be quenched by reducing the bias voltage below threshold, resetting the detector to allow for additional single photon detections after a certain dead time. These components for Geiger mode detection and quenching are combined in a single photon counting module (SPCM). Unfortunately, these detectors cannot typically distinguish between single photons and multiple photons, as any photon number more than one will trigger an avalanche detection. Simultaneous detection of two or more photon states can be done using multiple SPCM's with beamsplitters dividing a fraction of the beam into each one, and then conditioning on

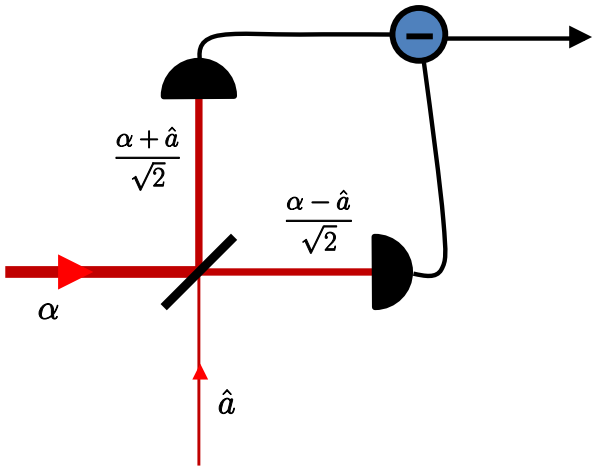

Figure 2.2: Homodyne detector. The photocurrents from one of the photodiodes is subtracted from the other, and the resultant signal is sent to the acquisition card.

trigger events in each detector.

2.4.3 Homodyne Detection

So far, the intensity and SPCM measurements only give information about the photon number distribution, which only gives the diagonal elements of the density matrix in the Fock basis. Due to this, these measurements cannot distinguish between the pure state $|\psi\rangle = \alpha|0\rangle + \beta|1\rangle$ and the mixed state $\rho = |\alpha|^2|0\rangle\langle 0| + |\beta|^2|1\rangle\langle 1|$, which differ in the off-diagonal terms of the density matrix that represent a coherent, fixed phase relation between the $|0\rangle$ and $|1\rangle$ components. However, the optical field oscillates at hundreds of THz, which is way beyond the capabilities of current detectors to measure directly. To get around this, we must take advantage of interference to cancel out any fast-oscillating terms at optical frequencies.

Balanced homodyne detection (BHD) is another clever detection technique that uses this interference idea to directly measure the phase-dependent quadrature distributions using a pair of photodiodes, at the same time amplifying the normally undetectable signal from a weak quantum state. The idea is shown in Figure 2.2. The incoming weak signal state is

interfered with a strong coherent state $|\alpha\rangle$ called the local oscillator (LO) on a 50:50 beamsplitter. The two outgoing beams are then detected by a pair of identical photodiodes, and the resulting photocurrents are subtracted from each other to give a final current which is proportional to the quadrature of the signal state along the phase defined by the phase of the coherent state. To see how this result comes about, we can see how the beamsplitter transformation and subsequent subtraction of the two modes affects the creation and annihilation operators of each mode. Defining the incident annihilation operator of the incident signal mode as $\hat{a}$ and of the incident coherent state as $\hat{b} = |\alpha|e^{i\theta}$, the outgoing modes of the beamsplitter are then:

$$\hat{a_1}' = \frac{1}{\sqrt{2}}(\hat{a} + |\alpha|e^{i\theta}) \tag{2.34}$$

$$\hat{a_2}' = \frac{1}{\sqrt{2}}(\hat{a} - |\alpha|e^{i\theta}) \tag{2.35}$$

The linear photodiode gives an output current that is given by $\hat{i}_{1,2} = g\hat{n}_{1,2}$ where g is the gain of the detector. Calculating the subtraction of the two currents gives:

$$\begin{aligned}
\hat{i}_{HD} &= \hat{i}_1 - \hat{i}_2 \\
&= g(\hat{a}|\alpha|e^{-i\theta} + \hat{a}^\dagger|\alpha|e^{i\theta}) \\
&= \sqrt{2}g|\alpha|(\hat{X}\cos(\theta) + \hat{P}\sin(\theta)) \\
&= \sqrt{2}g|\alpha|\hat{q}_\theta
\end{aligned} \tag{2.36}$$

In this way, we can see that the homodyne detector current is linearly proportional to the generalized quadrature $\hat{q}_\theta$, and that the normal detector gain is multiplied by the amplitude of the coherent state $|\alpha|$. Considering that $|\alpha|$ can be made very large using a bright coherent state, even very weak signal states with $\langle n\rangle < 1$ can be measured that would otherwise be too weak to detect using intensity measurements.

Of course, the derivation of Equation (2.36) is made under assumptions of ideal detector behavior and perfect overlap of the signal and LO beams, which is typically not quite the case experimentally. Any spatial or temporal mismatch between the signal and LO field,

which can arise from the two fields having a different transverse beam profile or misaligned k-vectors, may be quantified by the visibility $\mathcal{V}$. This $\mathcal{V}$ is defined by:

$$\mathcal{V} = \frac{I_{max} - I_{min}}{I_{max} + I_{min}} \tag{2.37}$$

where the maximum and minimum intensities are the result of constructive and destructive interference between two fields of equal intensities, as the phase of one of the fields is scanned. If there is perfect overlap, the ideal visibility of $\mathcal{V} = 1$ would be achieved, while increasingly worse overlap causes the visibility to decrease. Such mode mismatch degrades the measured signal from the ideal case. The effect of this mode mismatch can be modeled by the beamsplitter model of loss, where the signal is mixed with vacuum by a beamsplitter with transmission $T = \mathcal{V}^2$. An additional detrimental effect to consider is the imperfect quantum efficiency η of the homodyne detector photodiodes. This contributes a similar loss, with $T = \eta$ [42].

Another effect which is important experimentally is that the generated signal photons are not instantaneous and instead are distributed over a temporal mode $\phi(t)$. This can be understood as the instantaneous field operators $\hat{a}(t)$ acting over a distribution in time to give the combined operator $\hat{A}$, given by:

$$\hat{A} = \int_{-\infty}^{\infty} \hat{a}(t)\phi(t)dt \tag{2.38}$$

This $\hat{A}$ acts by annihilating a photon over the temporal mode $\phi(t)$. Note that the temporal mode $\phi(t)$ is normalized such that $\int_{-\infty}^{\infty} \phi(t)dt = 1$.

Equation (2.36) describes the instantaneous measurement of the signal field quadrature $\hat{q}_\theta(t)$, however for a signal state with a finite temporal profile $\phi(t)$ we need to find the

integrated quadrature $\hat{Q}_\theta$ in temporal mode of the photon:

$$\begin{aligned}\hat{Q}_\theta &= \hat{X}\cos(\theta) + \hat{P}\sin(\theta) \\ &= \Big(\frac{\hat{A}^\dagger + \hat{A}}{\sqrt{2}}\Big)\cos\theta + \Big(i\frac{\hat{A}^\dagger - \hat{A}}{\sqrt{2}}\Big)\sin\theta \\ &= \int_{-\infty}^{\infty}\Big[\Big(\frac{\hat{a}^\dagger + \hat{a}}{\sqrt{2}}\Big)\cos\theta + \Big(i\frac{\hat{a}^\dagger - \hat{a}}{\sqrt{2}}\Big)\sin\theta\Big]\phi(t)dt \\ &= \int_{-\infty}^{\infty}\hat{q}_\theta(t)\phi(t)dt \end{aligned} \tag{2.39}$$

This gives a single quadrature value for that signal state. The necessity for this integration is often ignored by matching the local oscillator temporal mode to be identical to the signal mode at all times, however this is not always practical. Using a continuous-wave local oscillator and integrating the quadratures following Equation (2.39) is much easier experimentally and functions for difficult-to-match temporal modes, which is the method we use in this experiment.

Non-instantaneous response of the homodyne detector complicates quadrature measurement even further. For a detector with a temporal response function $r(t)$, the actual response (as opposed to Equation (2.36)) becomes:

$$\hat{i}_{HD}(t) \propto \int_{-\infty}^{\infty}\hat{q}_\theta(t')r(t-t')dt' + \hat{i}_e(t) \tag{2.40}$$

where i_e gives the background electronic noise. The desired quadrature value can be found experimentally by integrating the measured HD current with a chosen temporal mode $\psi(t)$:

$$\begin{aligned}\hat{Q}_{meas} &= \int_{-\infty}^{\infty}\hat{i}_{HD}(t)\psi(t)dt \\ &= \int_{-\infty}^{\infty}\int_{-\infty}^{\infty}\hat{q}_\theta(t')r(t-t')\psi(t)dt'dt + \int_{-\infty}^{\infty}\hat{i}_e(t)\psi(t)dt \\ &= \int_{-\infty}^{\infty}\hat{q}_\theta(t')\psi'(t')dt' + \hat{Q}_e \end{aligned} \tag{2.41}$$

where $\psi'(t') = \int_{-\infty}^{\infty}\psi(t)r(t-t')dt$ and $\hat{Q}_e = \int_{-\infty}^{\infty}\hat{i}_e(t)\psi(t)dt$. By comparison with Equation (2.39), we can see that the effect of the HD response function is compensated for by choosing the integration mode $\psi(t)$ such that $\psi'(t)$ matches the actual temporal mode $\phi(t)$. This

can be challenging for an arbitrary temporal mode, however if the inverse bandwidth of the detector is much smaller than the time scale of the signal temporal mode, we can approximate $r(t)$ as a delta function. Any temporal mode mismatch that occurs by choosing the wrong temporal mode $\psi(t)$ results in losses similar to a spatial mode mismatch, with efficiency given by [48, 49]:

$$\eta = \frac{|\int_{-\infty}^{\infty} \psi'^{*}(t)\phi(t)dt|^2}{\int_{-\infty}^{\infty} |\phi(t)|^2 dt \int_{-\infty}^{\infty} |\psi'(t)|^2 dt} \tag{2.42}$$

We can also consider the effect of the electronic noise $\hat{Q}_e$ in the HD. We can quantify the equivalent loss due to electronic noise by comparing the signal and the electronic noise variances:

$$1 - \eta_e = \frac{\langle \Delta Q_e^2 \rangle}{\langle \Delta Q^2 \rangle} \tag{2.43}$$

The right hand side decreases with LO power, typically making the electronic noise negligible for high LO powers when using well-designed detectors. However, the LO power that can be used is limited by the saturation power of the detectors. For this reason, the LO is typically operated just under saturation. In the present experiment with a 15mW LO, over the bandwidth of the detector we achieve a clearance of 10-18dB over the electronic noise, which corresponds to η_e within the 0.90 to 0.98 range.

2.5 Maximum Likelihood State Reconstruction

From performing homodyne measurements, we get a set of marginal quadrature distributions $\Pr(q_\theta)$ for a range of phase angles θ. From these quadrature distributions, which are the projections of the Wigner function onto the axis determined by θ, we need to reconstruct the original state that produced them. Historically this has been done by inverting the Radon transform (2.31) numerically, akin to the computed tomography (CT) technique used in medical imaging, where a 3D object is reconstructed from a set of 2D projections of that object. Performing this inverse Radon transform on a given set of quadrature distributions here would give the Wigner function, from which the density matrix of the state can be

directly computed from Eq. (2.32). However, this approach suffers from several drawbacks arising from requirements of the numerical implementations such as needing low-pass filtering or individually sampling the density matrix elements. These requirements introduce a loss of accuracy and can result in unphysical density matrices with negative diagonal elements.

To avoid these drawbacks, another technique known as iterative maximum likelihood estimation can be used. Roughly, maximum likelihood estimates a density matrix known as the estimator and then calculates the likelihood that that density matrix would give the experimentally measured quadratures. This estimator is then iteratively modified in each step to give a better estimator with an increased likelihood function, and this process is repeated until the estimator gets satisfactorily close to the density matrix which maximizes the likelihood function. Convergence of this process is not guaranteed [50], however in our experience with experimental homodyne data, acceptable convergence is quickly obtained within a few hundred iterations. Furthermore, since the likelihood function is convex, if a maximum is reached then it must be the global maximum. The maximum likelihood technique also has the advantage that the estimator can be made to be a physical density matrix, with non-negative diagonal elements and a trace of 1. For a more detailed description of the maximum likelihood technique, see for example [51].

2.6 Qubits and Quantum Information

A qubit, or quantum bit, is the basic quantum logic state used for many protocols in quantum information. It is the quantum analogue to a classical bit, which can either be a logical 0 or 1 and is used by classical computer systems everywhere. The qubit on the other hand, can not only be a 0 or a 1 but it can any coherent superposition of 0 and 1, typically represented by the state $\alpha|0\rangle + \beta|1\rangle$ where $|\alpha|^2 + |\beta|^2 = 1$. This coherence allows for interference effects to take place when interacting multiple qubits together, which allows for quantum logic operations that are not possible classically [52]. Another feature of qubits is that

they can be entangled together, allowing for a set of qubits to express higher correlations than in possible in classical systems. Measurements performed on one qubit can project other entangled qubits onto certain states, which is necessary for quantum teleportation and quantum computation.

The types of systems that these qubits have been encoded upon is quite varied. Light in particular is quite appealing as a mediator for quantum information and quantum communication, as it can be transmitted between distant parties at the speed of light and there are existing techniques available to create, measure and manipulate optical states. Qubit states of light are often prepared where the qubit encoding is done in terms of different spatial states, different polarization states, and different Fock states.

Light, however, has its limitations in that it is not easy to store for significant amounts of time. Along this front, longer lived media more suitable to storage of quantum information are being developed and used [53]. Systems such as atomic ensembles, trapped ions, and superconducting circuits have all shown promise as candidates for storage of qubits. Efficient interaction between these storage systems and the carrier system used for transmission is crucial to developing quantum networks. In this thesis, we discuss developments on the interaction between a collective atomic system and light, to create and manipulate qubits in both the optical and collective atomic regime.

Unfortunately, all of these systems are susceptible to losses and the purity of qubits in any of these systems will degrade due to interaction with the environment. To quantify the quality of these impure qubits, we introduce a definition of *generalized efficiency* [54]:

$$\mathcal{E}(\hat{\rho}) \equiv \frac{\rho_{11}}{1 - |\rho_{01}|^2/\rho_{11}} \tag{2.44}$$

This generalized efficiency can be understood by considering transmission through a loss channel with transmittance T. The generalized efficiency is then the minimum T such that the experimentally observed state can be obtained from some other pure input qubit state through this loss channel. It has the properties that $\mathcal{E}(\hat{\rho}) = 1$ for pure states, $\mathcal{E}(\hat{\rho}) = 0$ for

the vacuum state, and that it cannot be increased by any linear optical processing [55].

Chapter 3

Four-Wave Mixing as a Source of Quantum Light

3.1 Four-Wave Mixing

To model the response of a dielectric material to an external electric field, a model of linear susceptibility is typically used, where

$$\mathbf{P} = \epsilon_0 \chi \mathbf{E} \tag{3.1}$$

with χ being the electric susceptibility of the medium (which for anisotropic materials may be a tensor). However for nonlinear materials, such as an atomic gas near resonance, terms involving a higher order response to the electric field must be taken into account [56]:

$$\mathbf{P} = \epsilon_0 \left(\chi^{(1)}\mathbf{E} + \chi^{(2)}\mathbf{E}\mathbf{E} + \chi^{(3)}\mathbf{E}\mathbf{E}\mathbf{E} + ... \right) \tag{3.2}$$

Here, $\chi^{(n)}$ represents a rank $n+1$ tensor describing the nth order nonlinear response of that medium.

The $\chi^{(2)}$ response is the dominant term in many nonlinear processes involving crystals, such as sum-frequency generation and spontaneous parametric down conversion (SPDC). However for systems possessing inversion symmetry, such as an isotropic atomic gas, this second order nonlinearity vanishes [56]. This leaves the $\chi^{(3)}$ term as the lowest order nonlinear term for atomic systems, and this term is what is responsible for four-wave mixing. It can be expanded out as:

$$\mathbf{P}_i(\omega_q) = \epsilon_0 \sum_{jkl} \sum_{mnp} \chi^{(3)}_{ijkl}(\omega_q, \omega_m, \omega_n, \omega_p) \mathbf{E}_j(\omega_m) \mathbf{E}_k(\omega_n) \mathbf{E}_l(\omega_p) \tag{3.3}$$

While the treatment of four-wave mixing so far has been general and (3.3) holds for any four-wave mixing process, we can simplify things by looking at the process used in this

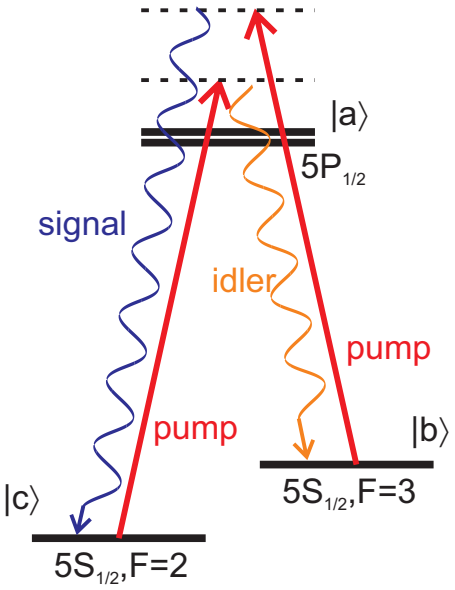

Figure 3.1: The three-level lambda system in ^{85}Rb. Optical pumping prepares most of the atoms in the $5S_{1/2}, F = 3$ state. A strong pump drives both the Raman transition to the $F = 2$ state and the subsequent Raman transition back to the $F = 3$ state. The probability of this second Raman transition returning the atoms to the original state is collectively enhanced along the phase-matched direction, leading to high-efficiency readout of the signal photon.

experiment, as shown in Figure 3.1. Here, the four-wave mixing process is driven by two pump photons with identical frequency and k-vectors. The resulting signal and idler photons are constrained by conservation of energy and momentum, which leads to a set of equations known as the *phase matching* conditions:

$$\omega_i = 2\omega_p - \omega_s \tag{3.4}$$

$$\mathbf{k}_i = 2\mathbf{k}_p - \mathbf{k}_s \tag{3.5}$$

Subscripts here indicate the idler, pump, and signal photons respectively. Furthermore, a specific frequency and spatial mode is selected for by experimental filters. Assuming that each of these modes is a collinear plane wave, we can write $\mathbf{E}_j(\omega_j) = \mathbf{E}_j e^{i(\mathbf{k}_j \cdot \mathbf{r} - \omega_j t)}$ and then the term responsible for the creation of the idler field from Equation (3.3) becomes:

$$\mathbf{P}_i(\omega_i) = \epsilon_0 \chi^{(3)}(\omega_i, \omega_p, \omega_p, \omega_s)\mathbf{E}_p^2(\omega_p)\mathbf{E}_s^*(\omega_s) \tag{3.6}$$

Since all of the beams are very nearly collinear and the atomic medium is isotropic, we can ignore the tensor nature of $\chi^{(3)}$ and treat $\mathbf{P}$ and $\mathbf{E}$ as scalars. We assume that the electric field can be modeled as a plane wave traveling in the z-direction with a slowly varying amplitude envelope $\mathcal{E}(z)$. Then, the electric field becomes $E_j(\omega_j) = \mathcal{E}_j(z)e^{i(k_j z - \omega_j t)}$ and we can rewrite Equation (3.6) as:

$$P_i(z,t) = \epsilon_0 \chi^{(3)} \mathcal{E}_p^2(z) \mathcal{E}_s^*(z) e^{i(k_i z - \omega_i t)} \tag{3.7}$$

where $\chi^{(3)} \equiv \chi^{(3)}(\omega_i, \omega_p, \omega_p, \omega_s)$ and frequencies are indicated by the subscripts.

To study the dynamics of the system, we can apply the electromagnetic wave equation

$$\left(\nabla^2 - \frac{1}{c^2}\partial_t^2\right) E = \frac{1}{\epsilon_0 c^2}\partial_t^2 P \tag{3.8}$$

and find a solution under a few assumptions. We assume that the slowly varying amplitude profile is in the steady state, that is $\partial_t \mathcal{E} = 0$. We also assume the paraxial approximation $\partial_z^2 \mathcal{E} << 2k\partial_z \mathcal{E}$. Furthermore we assume no depletion of the pump $\partial_z \mathcal{E}_p = 0$. Then by solving the wave equation we arrive at:

$$2ik_i \partial_z \mathcal{E}_i = -\frac{\omega_i^2}{c^2} \chi^{(3)} \mathcal{E}_p^2 \mathcal{E}_s^* \tag{3.9}$$

Simplifying and taking $\kappa = i\frac{\chi^{(3)}}{2k_i}\mathcal{E}_p^2 = i\frac{\chi^{(3)}}{2k_i \epsilon_0 c} I_p$ yields:

$$\partial_z \mathcal{E}_i = \kappa \mathcal{E}_s^* \tag{3.10}$$

Taking the same approach in terms of the signal instead of the idler yields:

$$\partial_z \mathcal{E}_s = \kappa \mathcal{E}_i^* \tag{3.11}$$

Combining equations (3.10) and (3.11) gives:

$$\partial_z^2 \mathcal{E}_s = |\kappa|^2 \mathcal{E}_s \tag{3.12}$$

$$\partial_z^2 \mathcal{E}_i = |\kappa|^2 \mathcal{E}_i \tag{3.13}$$

which can be solved to give:

$$\mathcal{E}_s(z) = Ae^{|\kappa|z} + Be^{-|\kappa|z} \tag{3.14}$$

$$\mathcal{E}_i(z) = A^*e^{|\kappa|z} - B^*e^{-|\kappa|z} \tag{3.15}$$

Rearranging these equations, replacing the constants A and B with the initial conditions $\mathcal{E}_{i,s}(0)$, and defining $|\kappa|z = \zeta$ gives:

$$\mathcal{E}_s(z) = \mathcal{E}_s(0)\cosh(\zeta) + \mathcal{E}_i^*(0)\sinh(\zeta) \tag{3.16}$$

$$\mathcal{E}_i(z) = \mathcal{E}_i(0)\cosh(\zeta) + \mathcal{E}_s^*(0)\sinh(\zeta) \tag{3.17}$$

While this derivation has been completely classical, by replacing the electric field amplitudes with annihilation operators we arrive at an output which follows the two-mode squeezing transformation (3.24). Interestingly, while the classical picture requires an input electric field into the signal or idler modes to see amplification, the quantum picture allows for the two-mode squeezing operator to act on vacuum inputs, spontaneously generating pairs of photons from the annihilated pump photons.

3.2 Hamiltonian to Two-Mode Squeezed Vacuum

To develop a quantum treatment of the two-mode squeezing transformation that occurs in this four-wave mixing process, we can start from the Hamiltonian governing the annihilation of two pump photons and creation of a signal and idler pair. This is given by [57]:

$$\hat{H} = i\hbar(\gamma'\hat{p}\hat{p}\hat{a}^\dagger\hat{b}^\dagger - \gamma'^*\hat{p}^\dagger\hat{p}^\dagger\hat{a}\hat{b}) \tag{3.18}$$

where $\hat{p}$ represents the pump annihilation operator, and $\hat{a}, \hat{b}$ act on the signal and idler respectively. Assuming a strong pump field with no pump depletion, we can treat the pump operators as constants to arrive at the more familiar two-mode squeezing Hamiltonian:

$$\hat{H} = i\hbar(\gamma\hat{a}^\dagger\hat{b}^\dagger - \gamma^*\hat{a}\hat{b}) \tag{3.19}$$

The evolution of $\hat{a}$ and $\hat{b}$ can then be found:

$$\begin{aligned}\frac{d\hat{a}}{dt} &= \frac{1}{i\hbar}[\hat{H}, \hat{a}] \\ &= \frac{1}{i\hbar}[i\hbar(\gamma\hat{a}^\dagger\hat{b}^\dagger - \gamma^*\hat{a}\hat{b}), \hat{a}] \\ &= \gamma[\hat{a}^\dagger, \hat{a}]\hat{b}^\dagger \\ &= -\gamma\hat{b}^\dagger \end{aligned} \tag{3.20}$$

similarly:

$$\begin{aligned}\frac{d\hat{b}^\dagger}{dt} &= \frac{1}{i\hbar}[\hat{H}, \hat{b}^\dagger] \\ &= -\gamma^*\hat{a}[\hat{b}, \hat{b}^\dagger] \\ &= -\gamma^*\hat{a} \end{aligned} \tag{3.21}$$

Differentiating (3.20) and substituting (3.21) gives:

$$\frac{d^2\hat{a}}{dt^2} = |\gamma|^2\hat{a} \tag{3.22}$$

which has solutions:

$$\hat{a} = A\cosh(|\gamma|t) + B\sinh(|\gamma|t) \tag{3.23}$$

From initial conditions we have $\hat{a}(t=0) = A$, $d\hat{a}/dt|_{t=0} = |\gamma|B = -\gamma\hat{b}^\dagger(0)$. Defining $\zeta = \gamma t$ and choosing ζ to be real, we arrive at the squeezing transformation:

$$\hat{a}(t) = \hat{a}(0)\cosh(\zeta) - \hat{b}^\dagger(0)\sinh(\zeta) \tag{3.24}$$

$$\hat{b}(t) = \hat{b}(0)\cosh(\zeta) - \hat{a}^\dagger(0)\sinh(\zeta) \tag{3.25}$$

$$\hat{a}^\dagger(t) = \hat{a}^\dagger(0)\cosh(\zeta) - \hat{b}(0)\sinh(\zeta) \tag{3.26}$$

$$\hat{b}^\dagger(t) = \hat{b}^\dagger(0)\cosh(\zeta) - \hat{a}(0)\sinh(\zeta) \tag{3.27}$$

We can reformulate this in terms of the squeezing operator $\hat{S}(\zeta) = e^{i\hat{H}t/\hbar} = \exp(\zeta^*\hat{a}\hat{b} -$

$\zeta\hat{a}^\dagger\hat{b}^\dagger$) and then act this on the two-mode state with vacuum inputs for the signal and idler:

$$\begin{aligned}\hat{S}(\zeta)|0,0\rangle &= \exp(\zeta^*\hat{a}\hat{b} - \zeta\hat{a}^\dagger\hat{b}^\dagger)|0,0\rangle \\ &= \frac{1}{\cosh(|\zeta|)}\sum_{n=0}^{\infty}(-e^{(i\arg(\zeta))}\tanh(|\zeta|))^n|n,n\rangle \\ &\approx |0,0\rangle - \zeta|1,1\rangle + \zeta^2|2,2\rangle + ... \end{aligned} \tag{3.28}$$

From Equation (3.28), it is apparent that the two-mode squeezing operator that occurs as a result of the four-wave mixing process always creates photons in pairs. When this is applied to vacuum, the resulting output is known as the *two-mode squeezed vacuum*, and it is a very useful state that is often the starting point for generating other quantum states experimentally. We will show this in Section 3.4.

3.3 Atomic Structure of Rubidium

The atomic system chosen for this experiment is rubidium-85. One of the primary advantages of using Rb is that as an alkali metal, it only has only one valence electron. This leads to a simple, hydrogen-like electronic structure which is easy to work with. Its lowest lying optical transition is the D1 line at 794.98 nm [58], which is convenient as there are cheap and easily accessible diode lasers available at that wavelength. Furthermore, Rb-85 has a ground state with two easily distinguishable levels that are split by a hyperfine splitting of 3.035 GHz. This ground state splitting is much easier to work with experimentally than the corresponding 6.8 GHz ground state splitting that exists in Rb-87. The excited state for Rb-85 also has hyperfine splitting, but the 361 MHz splitting is not large enough to be resolved within the Doppler broadening at 100°C. In this respect, our system is a good approximation to a three-level lambda system. Rubidium also has the advantage of having high vapor pressures, allowing for good optical depths in a narrow cell, with only moderate heating.

The energy level diagram is shown in Figure 3.2. The pump laser used in this experiment

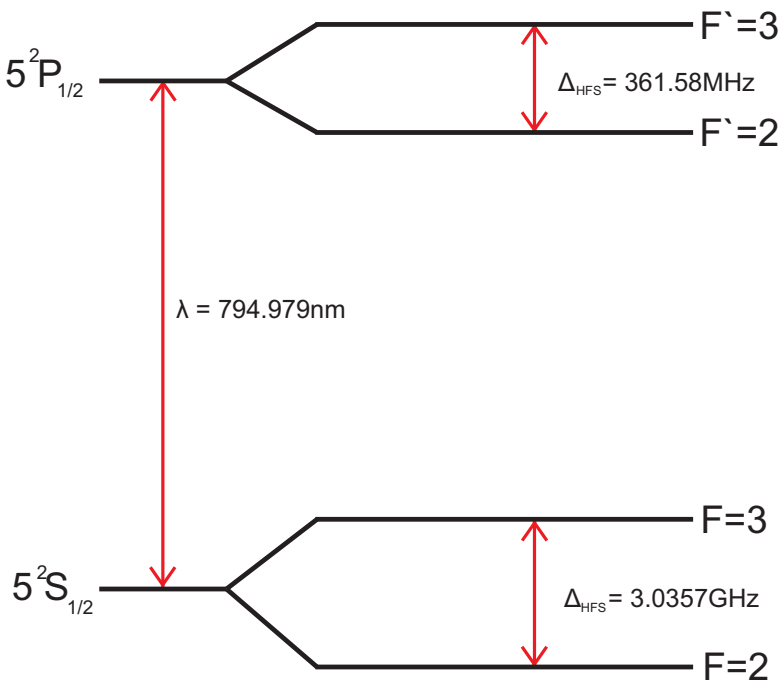

Figure 3.2: Energy level diagram with hyperfine splitting for the D1 transition in ^{85}Rb.

is 0.9 GHz detuned to the blue from the $|F = 2\rangle \rightarrow |F'\rangle$ transition. The idler photon is 3.078 GHz red-detuned from the pump, which corresponds to a two-photon detuning of about 43 MHz from the ground state detuning. Similarly, the signal photon is 3.078 GHz blue-detuned from the pump.

3.4 Experimental Single Photon Source

The first step in demonstrating the applicability of FWM as a quantum light source was to use it to experimentally generate and characterize one of the most basic nonclassical states of light - a single photon Fock state. Our goal for this part of the experiment was to not demonstrate that FWM can be used to produce these single photons, but that it can do it with high efficiency ($\geq$ 50 %) while simultaneously achieving relatively high generation rates and narrow spectral bandwidth in a pure spectral mode. However, there were several

challenges that needed to be overcome to achieve this. Of critical importance is that losses in the signal channel must be kept to an absolute minimum, and that the signal and idler states must be isolated from any background light (in particular the extremely bright pump beam).

The experimental design for the generation of single photons is shown in Figure 3.3. A 1W pump laser is generated from a Tekhnoscan TIS-SF 777 Ti:Sapphire laser. The primary fraction of this beam is passes through a Rb-85 cell which is heated in a homemade oven to approximately 107°C. Small fractions of the pump laser are split off before the cell for laser frequency stabilization, spectroscopy, and the generation of frequency shifted-beam using an acousto-optical modulator (AOM). The beam passing through the AOM is set up in a double-pass configuration such that the resulting output is 3.078 GHz red-detuned from the pump, corresponding to the frequency of the idler channel. We label this beam as the *seed* beam, and it serves the crucial role of allowing us to stimulate the FWM process for alignment purposes. When actually performing the experiment, the seed beam is blocked and the FWM process occurs spontaneously, resulting in the creation of a two-mode squeezed vacuum state with mean photon number much less than one. Of course, this light level is extremely inconvenient to detect, so when initially aligning the experiment the seed beam is injected along the idler channel to give a visible beam. It is overlapped with the pump beam inside the atomic cell at angle of approximately 5mrad, and the stimulated FWM process produces a conjugate beam along the signal channel at the signal frequency, which is also visible. These two beams allow for the simultaneous alignment of the signal and idler channels so that when the seed is turned off, what we are ultimately aligned to detect will be matched according to the FWM phase matching conditions.

After the cell, a quarter wave plate and a half wave plate rotate the polarization such that the pump beam is filtered out by two polarizing beamsplitters (PBSs). The signal and idler states, which are orthogonally polarized to the pump, continue on and are spatially separated

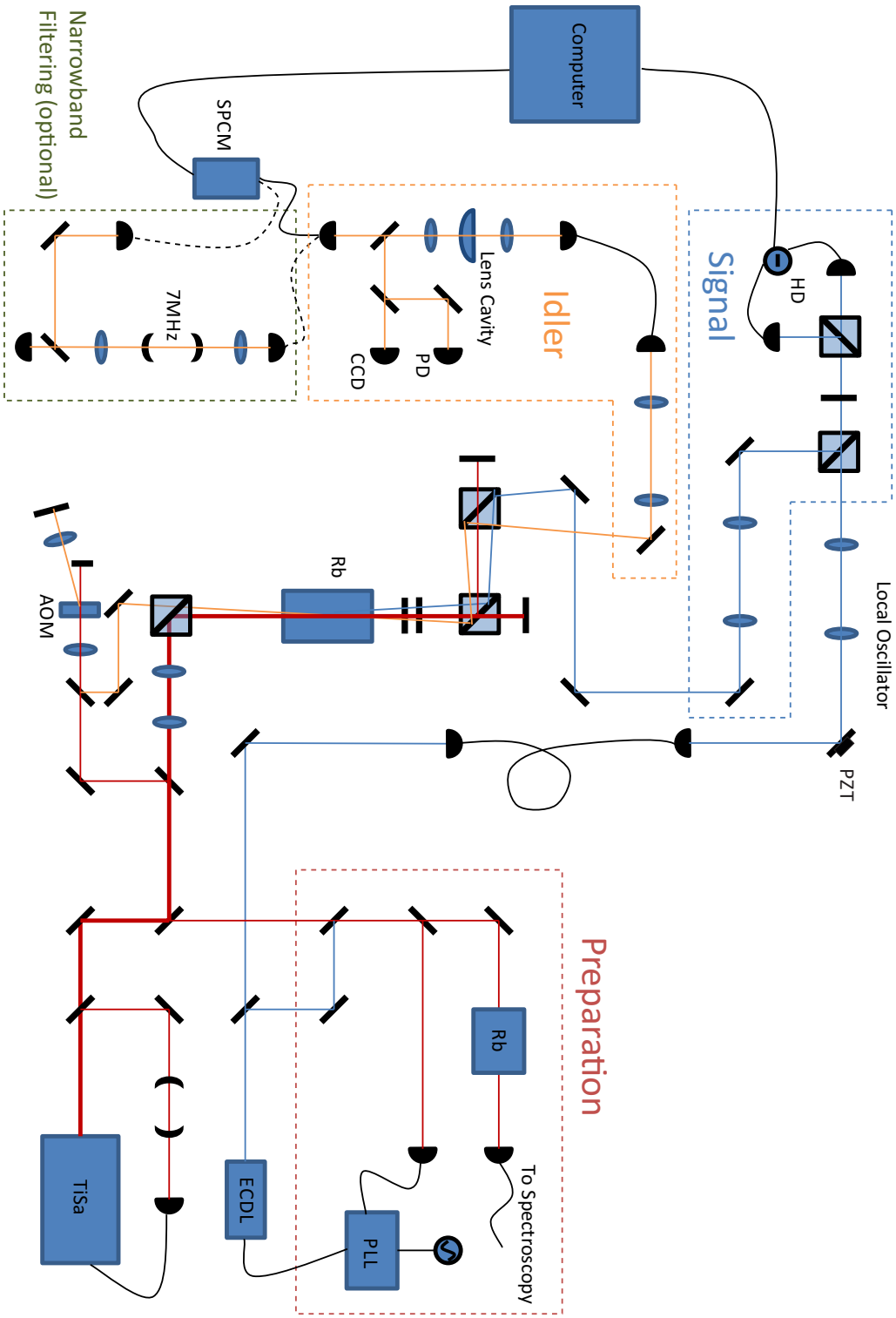

Figure 3.3: Experimental setup for generation of single photons and arbitrary qubits. The AOM path provides a weak coherent beam whose amplitude and phase relative to the LO can be controlled for the generation of arbitrary qubit states. An extra narrowbad filtering stage after the filtering of the idler by the lens cavity can optionally be used to extend the temporal profile of the signal photons.

by two pick-off mirrors. The signal channel is continuously monitored on a homemade 100 MHz homodyne detector [49], while the idler channel passes through several spatial and spectral filters before being detected by a SPCM. Both the HD and SPCM outputs are connected to an Agilent Acqiris DP214 digital acquisition card. Conditioned on a detection event in the SPCM, the HD current output is saved over a 90 ns temporal window. This 90 ns trace corresponds to one single detection event, and once the optimal temporal mode is determined, each trace is integrated with this temporal mode as described in Section 2.4.3 to give a single quadrature value. This process is then repeated 10^5 times per data run, to give sufficient statistics that a quadrature distribution can built up. Subsequently, the maximum likelihood algorithm is applied to reconstruct the state of the signal. Since single photons are phase-independent, we don't have to worry about the phase of the local oscillator, however a piezo-electric transducer (PZT) is attached to one of the mirrors in the LO path allowing for the controllable scanning of phase, which will be used for later experiments.

The generation of a phase-stable local oscillator at the frequency of the signal posed another challenge. Ideally, the LO would have a power in the range of 10mW to 20mW while being 3.078 GHz blue-detuned from the pump beam and simultaneously phase-stable to the pump. Use of a double-passed AOM similar to the seed beam could achieve this frequency shift and phase stability, however available AOMs at this frequency were only 1-2% efficient in the double-pass configuration and did not operate at such high powers. To solve this, a separate Toptica DL100 external cavity diode laser (ECDL) was installed at the desired frequency. Phase stability was achieved by measuring the beat signal between the LO and the pump, and locking that to a stable frequency reference using a homemade phase lock loop (PLL) [59].

Selection of a well-defined spatial mode for the signal and idler channels is crucial for efficient measurement. The phase matching conditions ensure that correlated photons are generated in pairs, on opposite sides of the the pump. However, the FWM process is spatially

multimode [60] so pairs of photons will be created in a cylindrically symmetric fashion around the pump with a fairly wide range of angles. To ensure that the measured signal and idler photons are correlated as strongly as possible, only a very narrow angular cross-section is allowed to be detected in the idler channel, and the corresponding signal is measured as the signal channel. This is accomplished by inserting a single-mode fiber in the idler path, which defines the spatial mode of the idler photons that we measure as the spatial mode of the fiber. This mode very closely approximates a TEM_{00} Hermite-Gaussian mode [61]. Detection along this narrow idler mode collapses the spatial mode of the signal to be conjugate to that of the idler, according to the Klyshko advanced wave model [62, 63]. We ensure that we only measure this conjugate signal mode by putting the local oscillator through an identical fiber to the one in the idler path, and then mode matching the two beams in terms of k-vector and in terms of Gaussian beam width and divergence in order to achieve maximum visibility.

A key factor to the success of this experiment is frequency filtering of both the idler and signal channels. The signal channel is inherently filtered by the reliance of homodyne detection on interference of the signal with the LO, and due to this only frequency components within a very small range around the LO will be measured. Frequency filtering of the idler is much more crucial, as the SPCM behaves essentially like a "white light" detector in that its response is essentially independent of frequency, at least within the frequency ranges that we are working with. To this end, a custom-designed monolithic Fabry-Pérot [64] cavity is employed in the idler channel with a FWHM of approximately 55 MHz and a off-resonant mode rejection of 48dB. The idler beam is mode-matched to the TEM_{00} mode with transmission of approximately 50%. The cavity transmission frequency is tuned to the idler frequency by adjusting the thickness of the cavity very slightly using temperature. The FSR of 23.1 GHz ensures that neither the signal or the pump frequencies are resonant, allowing for good isolation of the desired idler frequency.

Given a known temporal mode of the heralded photon would allow the use of Equation

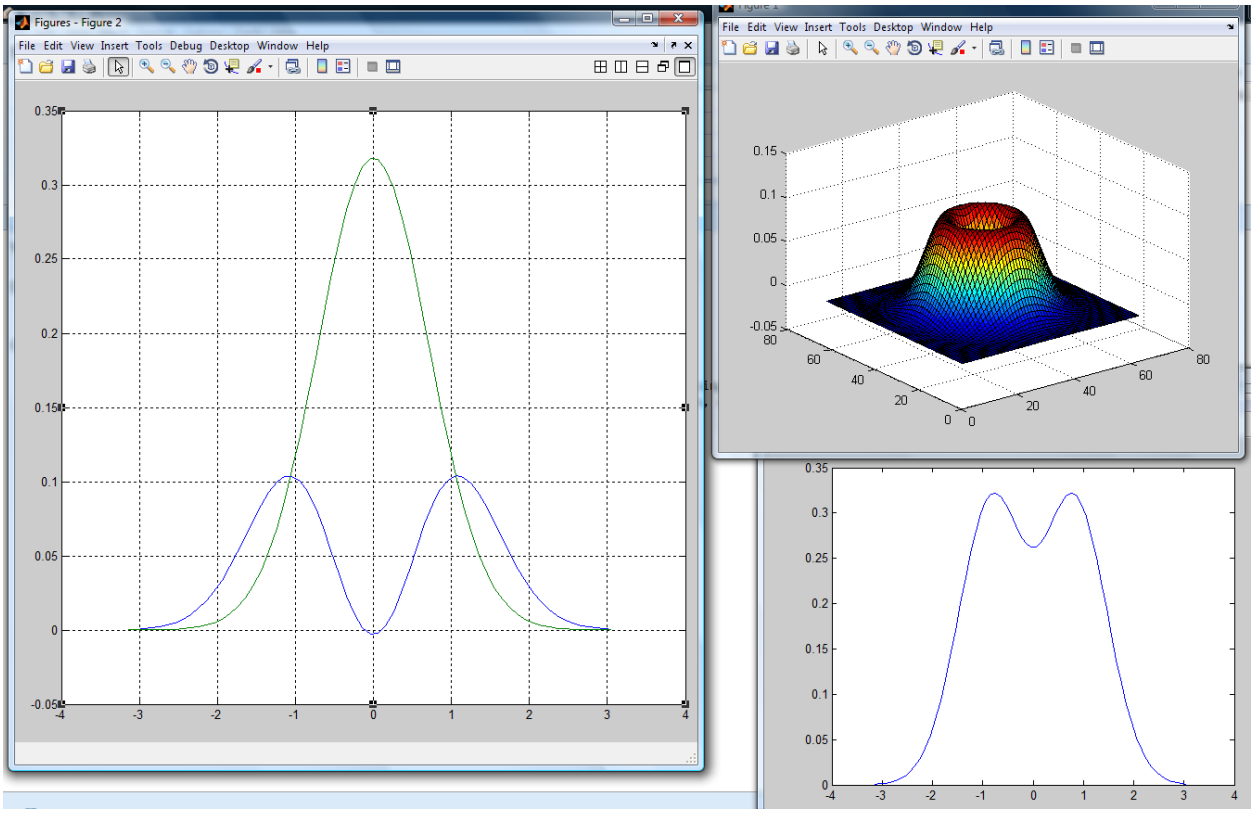

Figure 3.4: Maximum likelihood reconstruction of experimental data. The center slice of the Wigner function is compared to the vacuum distribution, shown left. Top right shows the Wigner function and bottom right shows the marginal distribution.

(2.41) to reconstruct the quadrature distribution. The determination of such temporal mode is non-trivial, and is discussed in detail in Section 3.5. However, once this temporal mode is determined then reconstruction of the state follows fairly simply. The raw homodyne current trace are integrated with the temporal mode to give the quadrature distribution and the MaxLik algorithm is used to reconstruct the density matrix most likely to reproduce the experimental data. From the density matrix, Equation (2.30) can be used to find the Wigner function. Results of this procedure are shown in Figure 3.4.

With this method of generating single photons, we achieved an uncorrected ρ_{11} density matrix element of 0.50 [1]. This is notable as it is roughly an order of magnitude higher than previous results from atoms, with no correction for experimental losses. The two photon component ρ_{22} is typically in the range of 0.05 to 0.07, which is somewhat high compared

to SPDC, although not that surprising considering our system. At the current temperatures the gain of our system is about 1.1, which contributes predominantly to this two photon component. Reducing the gain by decreasing the temperature would act by decreasing γ in Equation (3.19), which would decrease ρ_{22} at the cost of a significant decrease in count rate. Experimentally, we have also found this decreases the single photon efficiency, likely due to increased significance of SPCM dark counts and counts from scattered pump light that makes it through the filters. In the FWM system, Raman scattering of pump photons results in a thermal background, which contributes to the two photon component.

We can compare these results to the nonclassicality criteria that have been discussed in Section 2.3. While the squeezing criterion does not apply here, negativity of the Wigner function and the limits on ρ_{11} both show that our state is nonclassical. Having $\rho_{11} = 0.50$ does not make the Wigner function negative on its own (it would only decrease to 0 at the origin), however the small contribution from ρ_{33} is enough to make the Wigner function very slightly negative. A much better demonstration of nonclassicality comes from the ρ_{11} value itself, which classically can be no larger than $e^{-1} \approx 0.37$. The value that we achieved of $\rho_{11} = 0.50$ well surpasses that, thus the state we have created is nonclassical. Another figure, which is $g^{(2)}(0) \equiv \langle \hat{a}^\dagger \hat{a}^\dagger \hat{a} \hat{a} \rangle / n^2 = 0.51 < 1$ also shows nonclassicality.

Another important figure of merit for single photon sources is the *spectral brightness* $S(\nu)$, defined as the photon generation count rate per unit bandwidth. In the present experiment we achieve a count rate of 250000 counts per second, passing through a Fabry-Pérot cavity with FWHM of approximately 55 MHz. Several definitions have been used for whether the bandwidth used for $S(\nu)$ should consider the FWHM or the $1/e^2$ radius or the standard deviation, however for consistency we will use the FWHM. This corresponds to a spectral brightness of 4500 for our experiment.

3.5 Temporal Mode of Photons

The signal and idler photons before filtering are generated with a temporal mode that is determined by the Fourier transform of the FWM gain bandwidth. This gain bandwidth is quite dependent on the properties of the experimental system such as temperature, phase matching, pump intensity and pump detuning [65]. Values for Rb-85 have been reported that range from 20 MHz [65] in free-space squeezing experiments to 300 MHz [66] in photonic bandgap fibers. In the present experiment, we estimate this gain bandwidth by seeding the FWM process and observing the generated signal intensity as the seed frequency is varied. We find the FWM gain bandwidth to be approximately 50 MHz. Since this gain bandwidth is on the same scale as the filtering that we are performing, the frequency profile is the product of the two effects in the frequency domain. For simplicity here, we ignore the effect of the gain bandwidth and concentrate on the effect of the filtering on the temporal mode. In particular, the temporal mode of the heralded signal photon must be determined for accurate reconstruction of the signal state.

Assuming an infinite bandwidth for the FWM process, the two-mode signal and idler output state before any filtering is the following:

$$|\Psi\rangle = \int |\omega_s, \omega_i\rangle \, \delta(\omega_s + \omega_i - 2\omega_p) d\omega_s d\omega_i \tag{3.29}$$

where $|\omega_s \omega_i\rangle$ represent single-frequency (delta function) modes and the integration gives the (currently flat) frequency spectrum. The idler is then filtered via transmission through the lens cavity, which introduces a transmission factor $T = \frac{1}{1-2i\frac{\Delta}{\gamma}}$. Here, $\Delta = \omega_c - \omega_i$ is the detuning of the idler from the cavity frequency and γ is the cavity linewidth. After the lens cavity the two-mode state is then:

$$|\Psi\rangle = \int |\omega_s, \omega_i\rangle \, \frac{1}{1-2i\frac{\Delta}{\gamma}} \delta(\omega_s + \omega_i - 2\omega_p) d\omega_s d\omega_i \tag{3.30}$$

Next, the idler is detected by a SPCM, which we can assume to have perfect timing resolution (on the order of 50-100 ps). This collapses the state of the idler and projects the

signal onto a well-defined temporal mode. The instantaneous detection can be written as a delta-functioned state in time: $|t_i\rangle = \int |\omega_i'\rangle\, d\omega_i' e^{i\omega_i' t}$. Acting this on the idler state at $t = 0$ leaves the resulting signal temporal mode:

$$|\psi_s\rangle = \langle t_i = 0|\, \Psi'\rangle = \int |\omega_s\rangle\, \frac{1}{1 + 2i\frac{\Delta_s}{\gamma}} d\omega_s \tag{3.31}$$

In the last step, we define $\Delta_s = (2\omega_p - \omega_c) - \omega_s = -\Delta$, which can be understood as the detuning of the signal from the central cavity frequency reflected about the pump frequency.

Now let $\omega_s = \omega_0 + \Delta_s$, then

$$|\omega_s\rangle = \int |t\rangle\, e^{-i\omega_0 t} e^{-i\Delta_s t} dt \tag{3.32}$$

Substituting this into Equation (3.31) we get

$$|\psi_s\rangle = \iint |t\rangle\, e^{-i\omega_s t} \frac{1}{1 + 2i\frac{\Delta_s}{\gamma}} dt d\omega \tag{3.33}$$

$$= \int |t\rangle\, \phi(t) e^{-i\omega_0 t} dt \tag{3.34}$$

where

$$\phi(t) = \int \frac{e^{-i\Delta_s t}}{1 + 2i\frac{\Delta_s}{\gamma}} d\omega \tag{3.35}$$

can be recognized as the temporal mode. Evaluating the complex integral we get:

$$\phi(t) = \begin{cases} Ce^{\gamma t/2} & \forall\ t < 0 \\ 0 & \forall\ t > 0 \end{cases} \tag{3.36}$$

For the experimental values of $\gamma = 2\pi \times 64$ MHz $\approx 4 \times 10^8 \mathrm{s}^{-1}$, this works out to:

$$\phi(t) = e^{\frac{t}{5\mathrm{ns}}} \Theta(-t) \tag{3.37}$$

where $\Theta(-t)$ is the Heaviside step function.

This one-sided exponential profile has some quite sharp features, however due to the finite response function of the homodyne detector and the gain bandwidth of FWM, these

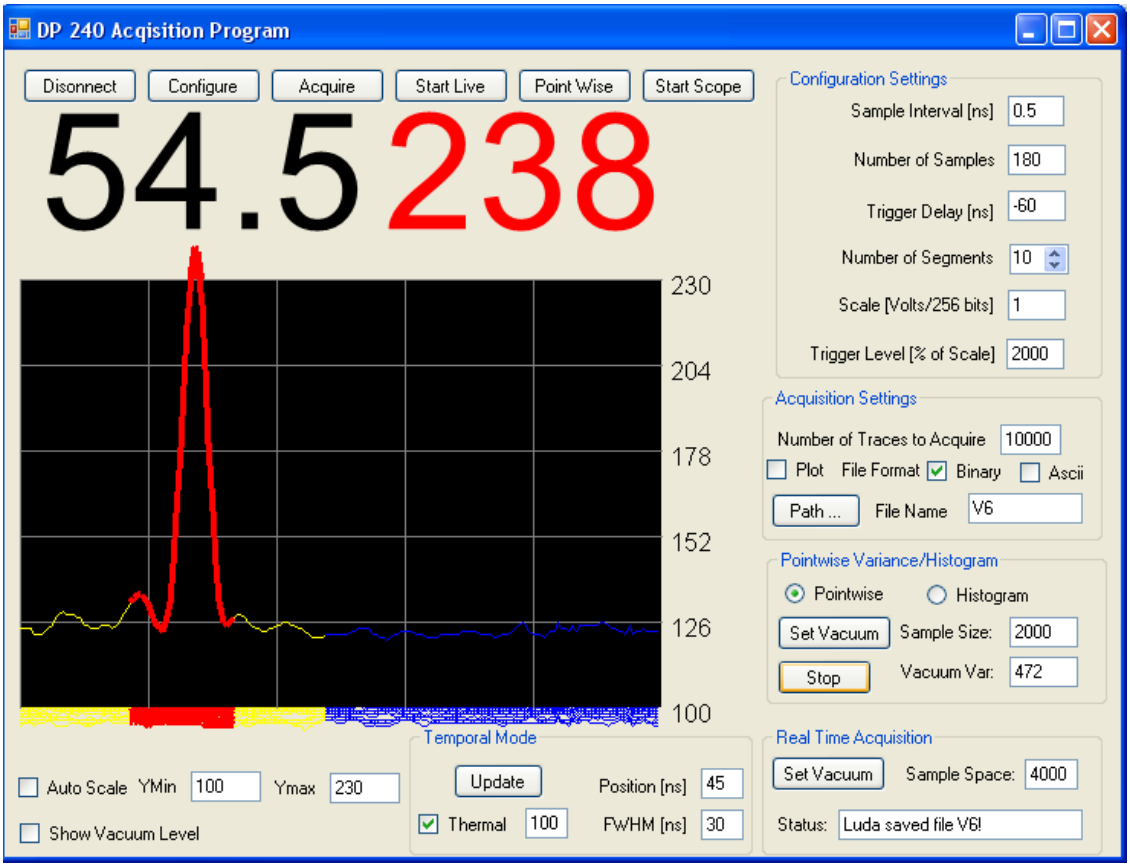

Figure 3.5: Homemade software allows us to monitor the pointwise variance as a function of time, which was crucial to the alignment of the experiment.

features tend to be smoothed out to a more Gaussian shape. The exponential time constant of around 5 ns is also on the same order as the width of the homodyne response function (which has an inverse bandwidth of around 1.75 ns). While a good choice of reconstructed temporal mode helps to reduce the influence of the HD response function, measuring near the limit of the detector undoubtedly causes losses [49] due to noise and uncertainties. Still, we can still try to infer the best temporal wavefunction by several methods. The first is to look at the pointwise variance for each of the time bins recorded by the digital acquisition card. Since a single photon state has three times the quadrature variance than vacuum, the time bins with increased variance show where the single photon measurement was most likely. This is shown in Figure 3.5, where pointwise variance is plotted as a function of time. Vacuum variance is normalized to 100 by blocking the signal state. The unblocked variance

is shown in the figure, which reaches 238 at its peak. The background variance is also increased to around 120 due to the presence of uncorrelated thermal background counts. We developed a homemade software interface which allowed us to monitor this in real time, which was crucial to the alignment of the experiment. This pointwise variance function serves as a starting point that could be used as a guessed temporal mode to reconstruct the signal state. From there, small modifications to the shape of the guessed temporal mode can be made to improve the reconstructed single photon component. Figure 3.6 shows reconstruction of the state using a temporal mode that consists of several superimposed Gaussians. The pointwise variance is shown in blue, while the optimized guessed temporal mode is shown in red.

Another much more promising method to determine the temporal mode is from the autocorrelation matrix defined by $A_{jk} = \langle i(t_j) i(t_k) \rangle$ [67]. It can be shown (see Appendix A) that the autocorrelation matrix is related to the density matrix in the time-bin basis by the following relation (assuming no detuning of the LO and instant HD response):

$$\hat{A} = \mathrm{Re}(\rho) + \frac{1}{2}\mathbb{1} \tag{3.38}$$

By removing the autocorrelation matrix of a randomly triggered background measurement from the autocorrelation matrix of the single photon, we were able to isolate the effect of the single photon. This also subtracts out the effect of the identity matrix. We then diagonalized the resulting matrix and took its primary eigenvalue. The diagonalization leaves the density matrix in the form:

$$\hat{\rho}' = \sum_i P_i |\psi_i\rangle\langle\psi_i| \tag{3.39}$$

for some temporal mode vectors $|\psi_i\rangle$. The primary eigenvalue, whose eigenvector corresponds to the temporal wavefunction, was roughly 50 times larger than any other eigenvalue indicating a highly pure temporal mode. From there we reconstructed the state in the Fock basis via the usual method of integrating the photocurrent with the temporal mode to get the quadratures and then using MaxLik to find the Fock-basis density matrix.

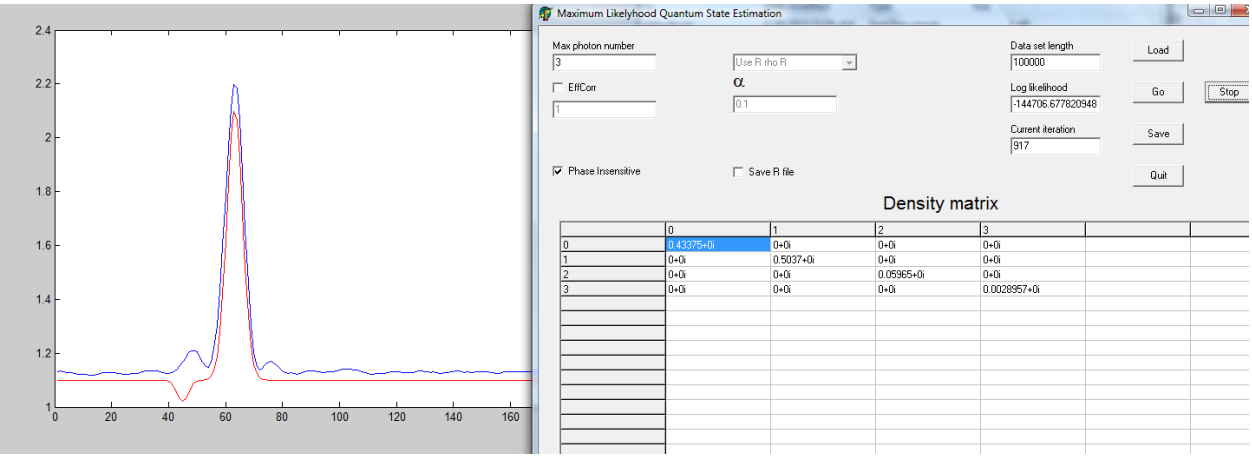

Figure 3.6: Reconstruction of the signal state is done by inferring a temporal mode to integrate over, producing a quadrature distribution. Maximum likelihood is then performed on this distribution, outputting the density matrix that is most likely to generate the measured data.

Experimentally, the response function of the homodyne detector quite significantly distorted the shape of the temporal mode. The predicted one-sided exponential function appears significantly rounded and almost Gaussian in Figure 3.6. Reconstruction with guessed temporal modes yielded approximately the same efficiency as using the method of autocorrelation or applying a genetic algorithm to find the temporal mode. This suggests that the temporal mode mismatch due to the limited resolution of the homodyne detector may be a limiting factor to efficient state reconstruction. To avoid this, a faster HD or narrower filtering may be used. Preliminary results towards implementation of a narrowband filter cavity into the idler channel are discussed in Section 4.4.

Chapter 4

Quantum State Engineering

4.1 Conditional Measurements on Light

In the previous chapter we have described the generation and characterization of one of the most basic quantum states - the single photon Fock state. However the two-mode squeezed vacuum state that we started out with initially before projecting the state onto the single photon state has many more components than just $|1\rangle$. Following the technique of Bimbard et al. [20], we can generate much more complicated states. Ultimately using this technique, we could generate any arbitrary single mode state:

$$|\psi\rangle = \sum_{n=0}^{N} c_n |n\rangle \tag{4.1}$$

The idea proceeds as follows: consider first the two-mode squeezed vacuum state given by Eq. (3.28). By heralding on exactly n photons in the idler channel, the signal is projected on the state $|n\rangle$. This allows for the generation of Fock states, which we used to prepare the single photon state. However, we can access not only Fock states but also superpositions of Fock states by clever use of an auxiliary classical state. Suppose we interfered the idler channel with a weak coherent state of controllable amplitude and phase before detection. Now if we detect n photons, we cannot tell if those n photons came from the idler, or if $n-1$ came from the idler and 1 came from the coherent beam, and so on. Assuming that we have properly interfered the idler and auxiliary states, the photons after interference are quantum mechanically indistinguishable. Thus, we cannot determine which photons originated from which source and as a result we end up with a weighted superposition of all possible combinations. Since the signal and idler channel must have an identical number of photons, this projects the signal state onto that very same superposition of Fock states.

Furthermore, the amplitude and relative phase between the Fock states are controlled by the amplitude and phase of the coherent beam, which is easily manipulated experimentally. To see how this works for a qubit, consider the combination of a weak two-mode squeezed vacuum $|\psi\rangle \approx |0_s, 0_i\rangle + \gamma|1_s, 1_i\rangle$ with a weak coherent state $|\alpha\rangle \approx |0_\alpha\rangle + \alpha|1_\alpha\rangle$. The three-mode state after interference of the idler with $|\alpha\rangle$ on a 50 : 50 beamsplitter is, to first order:

$$|\Psi\rangle_{after} \approx |0_s, 0_i, 0_\alpha\rangle + \frac{\gamma}{\sqrt{2}}\Big(|1_s, 1_i, 0_\alpha\rangle + |1_s, 0_i, 1_\alpha\rangle\Big) + \frac{\alpha}{\sqrt{2}}\Big(|0_s, 0_i, 1_\alpha\rangle - |0_s, 1_i, 0_\alpha\rangle\Big) \tag{4.2}$$

Heralding upon $|1_\alpha\rangle$ yields the (unnormalized) separable $|\psi_s\rangle \otimes |0_i\rangle$ state:

$$\Big(\frac{\alpha}{\sqrt{2}}|0_s\rangle + \frac{\gamma}{\sqrt{2}}|1_s\rangle\Big) \otimes |0_i\rangle \tag{4.3}$$

By controlling the amplitude and phase of $|\alpha\rangle$, any arbitrary signal cubit can be generated using this technique.

We can ultimately achieve the required degrees of freedom necessary to generate any arbitrary state with up to N photons by using N such coherent states and N single photon detectors. Following the setup of [20] the signal coefficiencts for $N = 2$ can be expanded out as follows:

$$|\psi\rangle = \Big(-\frac{\alpha^2}{2\sqrt{2}} + \frac{\alpha\beta}{2}\Big)|0\rangle + \frac{\beta\gamma}{2}|1\rangle + \frac{\gamma^2}{2}|2\rangle \tag{4.4}$$

where α and β describe the auxiliary coherent states and $\gamma \equiv \tanh(\zeta)^2$ describes the squeezing parameter of the two-mode squeezed vacuum. The ability for arbitrary control over all parameters comes at the cost of increasing complexity and decreasing count rates as N increases, however many quantum information protocols only require qubits ($N = 1$) or qutrits ($N = 2$) in which case this technique functions very well.

4.2 Application to Generating Optical Qubits

The next logical step after experimentally generating single photons was to extend the setup to be able to generate qubits [2]. Conveniently, we already had available to us a coherent beam at the idler frequency in the AOM-shifted pump beam that we used as the seed beam. To get to have a comparable mean photon number to our idler, we had to attenuate the beam to the level of 10^{-13} W. This was achieved through the use of several neutral density filters and several nearly minimized waveplate/PBS combinations. This heavily attenuated beam was then sent along the idler channel and overlapped such that it passed through the same single-mode fiber and Fabry-Pérot cavity as the idler. A conceptual experimental diagram is shown in Figure 4.1. The resulting signal state was then reconstructed similar to the procedure used in the single photon case. Unfortunately at such low power level it was difficult to directly measure the intensity as we could not directly measure the power using a power meter. However, with the SPCM turned on we could measure the increase in count rate from the presence of the coherent beam. We could also adjust the power using a half-wave plate followed by a PBS. Figure 4.2 shows that the count rate scales linearly with $\sin^2(\theta)$ as one would expect from Malus' law, indicating that the SPCM count rate serves as a valid measure of the relative intensity between the unseeded idler and combined seed+idler beams.

An added complication that is introduced to this experiment compared to the generation of single photons is the dependence on phase. The relative phase between the coherent seed beam and the local oscillator determines the relative phase between $|0\rangle$ and $|1\rangle$ in the signal qubit. Fortunately, the mean quadrature value varies proportionally to $\cos(\theta)$. This allowed us to infer the phase by taking a running average of the mean quadrature over several hundred consecutive data points, and then applying the arccos function. A PZT was placed in the LO path, which allowed us to controllably scan the phase over a 2π range.

The experimental results of this are plotted in Figure 4.3. The single photon Fock state

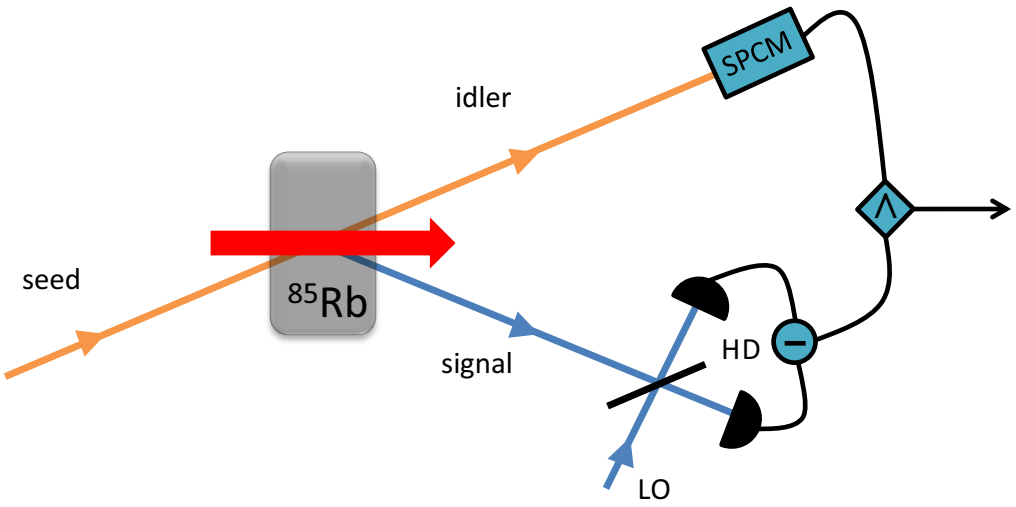

Figure 4.1: Conceptual qubit generation setup.

is compared to a generated qubit where 24% of the counts are coming from $|\alpha\rangle$. In the latter case, the off-diagonal element ρ_{01} arises, demonstrating coherence between the $|0\rangle$ and $|1\rangle$ components which does not exist in the case of the (lossy) single photon. Figure 4.4 plots the density matrix elements ρ_{11} and ρ_{01} as a function of increasing count rate from the coherent seed beam $|\alpha\rangle$. The blue circles show experimental data points while the black curve shows theoretical predictions matching our experimental parameters. Also plotted in Figure 4.4 is the generalized efficiency $\mathcal{E}(\hat{\rho})$, which describes the quality of the generated qubits and is defined by Equation (2.44) [54]. Ideally the generalized efficiency would be independent of the relative intensity of the idler and $|\alpha\rangle$, however experimental conditions such as higher order photon states and imperfect detection efficiency introduce some dependence. Furthermore, the non-perfect fit indicates there is some experimental decoherence which degrades the off-diagonal elements ρ_{01}. When the predicted ρ_{01} elements are reduced by a constant factor of 0.81, shown in the orange curve, this shows very good agreement with the experimental results. Ultimately, the source of this decoherence could not be directly isolated, however

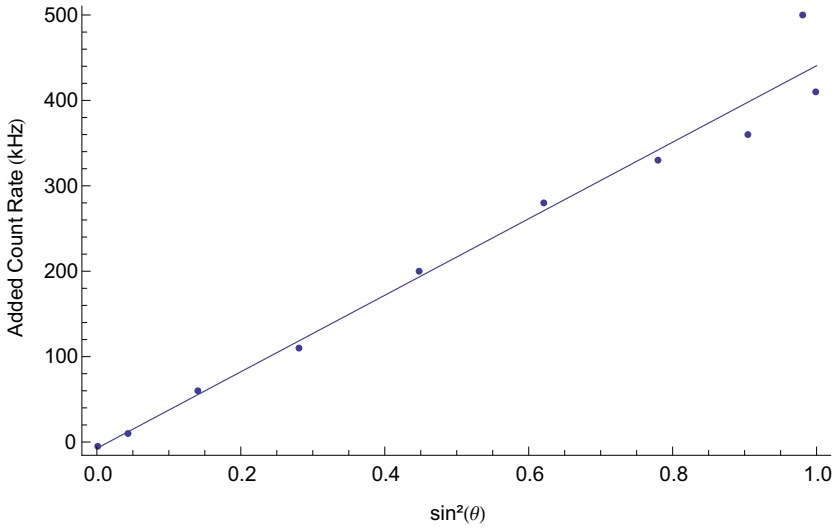

Figure 4.2: Increased count rate as a function of seed waveplate angle.

experimentation has managed to rule out mode-matching, optical losses, and any thermal background. Possible sources of this decoherence are discussed in the next section (4.3).

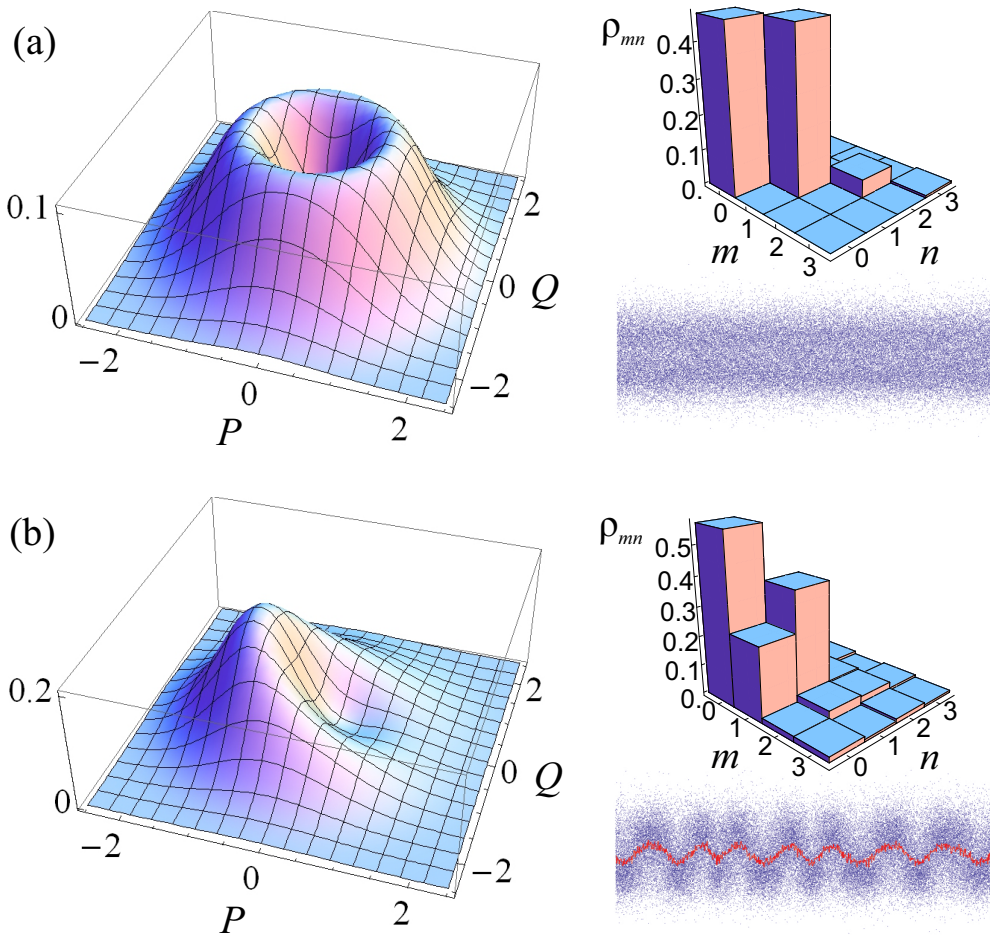

Figure 4.3: Reconstructed quantum states. (a) The single photon Fock state obtained in the absence of the seed ($\alpha = 0$). The Wigner function shows a clear dip at the origin, with the density matrix having a 47% single photon component. The quadrature data shows no phase dependence and has a reduced probability of measurement near zero, characteristic of single photons. (b) Reconstructed state for a generated qubit, in the case where 24% of the photon detection events are coming from $|\alpha\rangle$. The displacement of the peak of the Wigner function from the origin, along with the off-diagonal elements of the density matrix, show the presence of coherence between the single-photon and vacuum terms. The mean value of the measured quadrature oscillates as we scan the phase of the LO in time. Despite the significantly increased vacuum component, the off-diagonal terms contribute to a generalized efficiency of 46%.

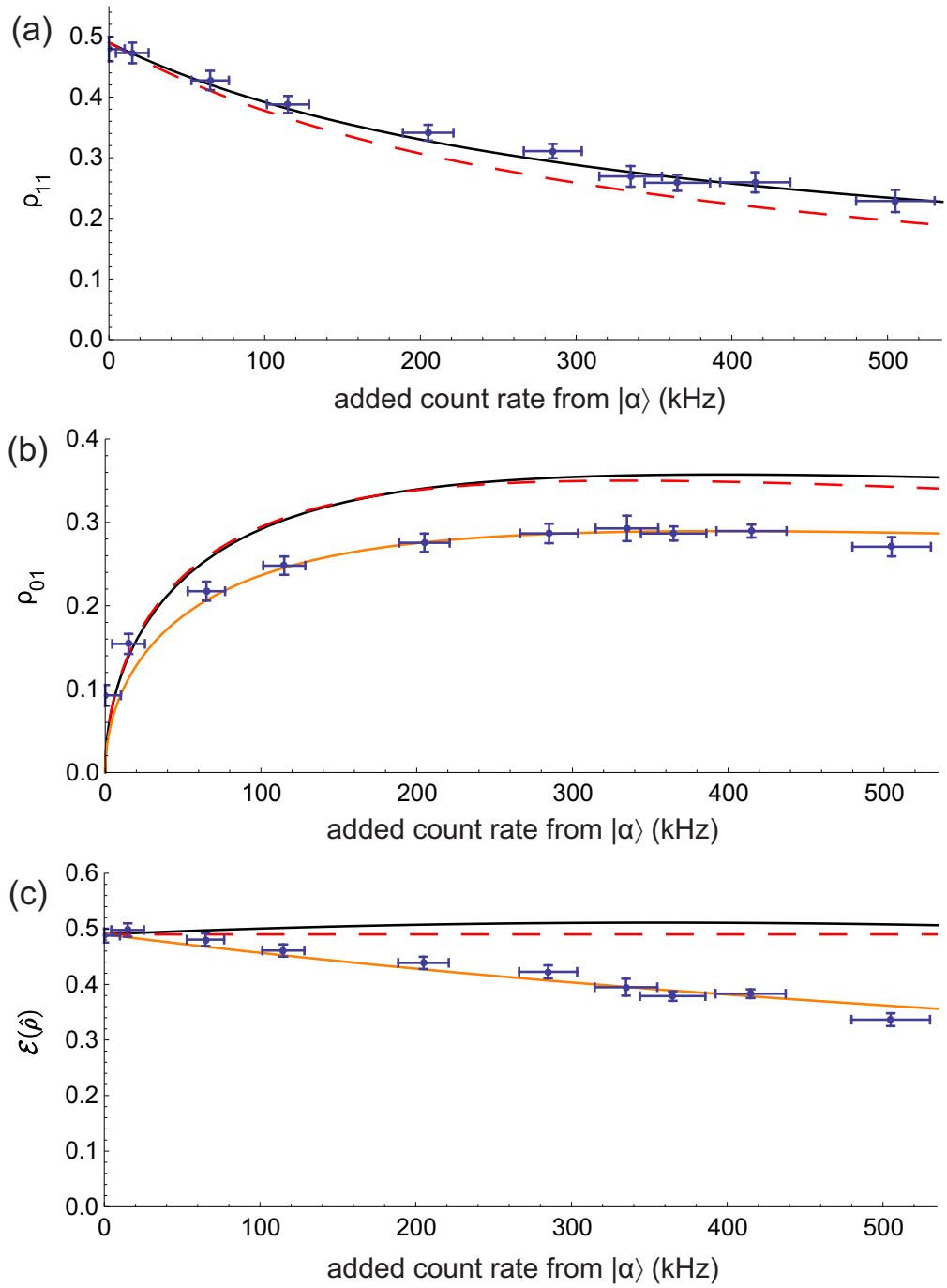

Figure 4.4: Experimental results. Density matrix elements (a) ρ_{11} and (b) ρ_{01} are shown, each as a function of the added count rate in the idler channel corresponding to increasing intensity of the seed coherent state. (c) The generalized efficiency $\mathcal{E}(\hat{\rho})$ is calculated over the same range of $|\alpha|$. The black solid line is generated using a theoretical model considering experimental imperfections. The dashed red curve uses a simplified model considering only the first order of the FWM Hamiltonian, neglecting photon number elements above $n = 1$. The orange curve considers a reduction of ρ_{01} by a constant factor of 0.81 with respect to the black curve.

4.3 Modeling of Losses and Experimental Imperfections

When initially interpreting the experimental data shown in Figure 4.4, a very simplified model considering only the first order of the FWM Hamiltonian (3.19) seeded by $|0\rangle_s \otimes |\alpha\rangle_i$ was used. Evolution under this Hamiltonian followed by single photon detection in the idler yields the state $|\psi_s\rangle = \alpha|0\rangle + \gamma t|1\rangle$ where $\zeta = \gamma t$ is a fixed constant related to the FWM gain. Subsequent loss in the signal channel are then modeled using the beamsplitter model of loss [42]. The results of that model are plotted as the dashed red line in the figure. By measuring the relative count rate between the vacuum-seeded idler and the added count rate when a coherent beam was overlapped with idler, it was possible to determine the relative intensity between $|\alpha\rangle$ and the signal photons coming from FWM. This left the only free parameter in the model to be the combined losses in the signal channel, which was estimated to correspond to transmission efficiency $\eta = 0.48$. Optical losses along the signal channel are easy to measure experimentally, however losses occuring before the signal leaves the rubidium cell, losses due to inefficient detectors, and losses due to mismatched spatial and temporal modes are more challenging to determine. This leaves determination of η from experimental conditions quite uncertain. By finding the parameter which best fit the experimental data, a value of $\eta = 0.48$ was determined. Even still, the predicted values for ρ_{01} were higher than the experimental data by a constant factor of around 25 %. In an attempt to understand the source of this discrepancy, a more detailed model (black curve in Figure 4.4) was developed. This model has the ability to include non-ideal SPCM efficiency, background thermal noise, higher order photon number components, and possible non-linear interaction by passing $|\alpha\rangle$ through the cell instead of overlapping the beams afterwards.

The model show in the black curve was again developed by starting with the FWM Hamiltonian (3.19) in Mathematica. The evolution operator $e^{i\hat{H}t/\hbar}$ is calculated up to $n = 4$, with $\zeta = \gamma t$ as a constant, free parameter. To calculate the unseeded FWM output, this evolution operator is applied to the two-mode vacuum state, resulting a two-mode squeezed

vacuum output (3.28). The coherent state $|\alpha\rangle$ is again introduced into this calculation by setting the input to the FWM as $|0\rangle_s \otimes |\alpha\rangle_i$. Losses in the idler channel are now considered, and applied using the beamsplitter model of loss, with $\eta_{idler} = 0.1$ used to estimate experimental conditions. The SPCM is modeled as a positive-valued operator measure (POVM) [68]. SPCM dark counts are also included into the POVM for completeness, however from the experimental count rates we determined that dark counts are insignificant. The action of this POVM collapses the two-mode state consisting of the signal and idler to just the single-mode signal state. Losses in the signal state are then applied, again using the beamsplitter model of loss. The effect of temporal and spatial mode mismatch, along with imperfect detection efficiency and optical losses can all be shown to follow this model [49, 48], and are thus combined into a single loss parameter η_{signal}. This results in the final signal density matrix, which we assume is efficiently measured. The relative count rate with or without $|\alpha\rangle$ is determined by performing the partial trace over the signal channel (pre-losses), then applying idler losses and comparing the resulting trace $\mathrm{Tr}[\hat{\mathrm{POVM}} \cdot \hat{\rho}_{idler}]$ with and without $|\alpha\rangle$.

These changes gave us more confidence in our model, as it now includes higher order photon number components, accounts for any non-linear interaction that occurs between $|\alpha\rangle$ and the FWM process, and accurately describes the effect of losses and inefficient detection in the idler channel. However, the resulting fit to experimental data still did not improve for any choices of ζ, η_{signal}, and η_{idler}, so we were able to conclude that some other effect was occuring. One theory was that there was a significant amount of uncorrelated thermal background light that was contaminating the signal and idler states. This idea had some promise in that a thermal state has no off-diagonal elements while it retains some diagonal elements. Thus, by mixing thermal states with our current signal and idler states, the off-diagonal elements would be reduced more than the diagonal elements, allowing for a better fit to experimental data. It is also quite reasonable that this thermal background exists in

our experiment, as the atoms are quite hot at $\sim 107°$C and exhibit fairly bright Raman scattering. This thermal background is implemented into the model by sending independent thermal states as inputs to the FWM process instead of vacuum states.

By adjusting the temperature of the thermal states in the model and corresponding adjusting ζ, η_{sig}, and η_{idl}, we were able to improve the fit of the model for ρ_{11} and ρ_{01}. However, with this many free parameters the optimal results started to become quite unphysical. The first sign of this was the ρ_{22} parameter, which experimentally was found to be $\rho_{22} = 0.06$ when $\alpha = 0$. However, the best fit parameters gave $\rho_{22} = 0.12$, which indicated there was way more thermal state in the model than the experiment. Furthermore, the percentage of count rates coming from the thermal state was over 30 %. Since this seemed quite unreasonable, we decided to estimate the proportion of thermal from the experimental ρ_{22} parameter and the experimental increase in variance when comparing a vacuum state to an randomly-triggered thermal state. From this, we determined much more reasonable parameters to use for the thermal state which contributed to only a small effect on the fit for ρ_{11} and ρ_{01}, and contributed to 7% of the SPCM counts. This thermal effect is included in the plots for Figure 4.4, and improves the fit slightly, although it still does not completely account for the discrepancy in the values for ρ_{01}.

The remaining discrepancy indicates there is some source of decoherence between the $|0\rangle$ and $|1\rangle$ components that is unaccounted for by our model. One possible source of this decoherence is some distinguishability between idler photons coming from $|\alpha\rangle$ and from FWM. In princible, these should be spatially indistinguishable as they both pass through the same spatial mode of a single mode fiber and then through the same spatial mode of the filter cavity. However, it is possible that they are not perfectly matched to this mode and there could be some very small mismatched transmission through other spatial modes. In the polarization basis, both beams pass through the same ports of several PBS cubes, and should also be well matched. Spectrally, the beams should also be indistinguishable in

principle due to the very fast timing resolution of the SPCM. This causes a quantum erasure [69] of any bandwidth information. Using a SPCM response of 50 ps, this should allow for bandwidth mismatches of up to 20 GHz. Another possible source of this decoherence is that our method of estimating the phase from the running average of the quadrature value is not precise enough. This would introduce some phase uncertainty in each quadrature point, which would cause some partial phase averaging in the maximum likelihood reconstruction. Althrough our model did not result in the complete description of where this decoherence comes from, its development has allowed us to gain insight into the effects of higher order photon states, thermal background, and losses from all sources. Furthermore it has allowed us to rule out these effects as the sole source of the discrepancy shown for ρ_{01}.

4.4 Controlling the Temporal Mode

In order to avoid the negative effects of the limited temporal resolution of our homodyne detector, we have implemented a 7 MHz bandwidth filter cavity into the idler channel. This Fabry-Pérot cavity is formed using two high-reflectivity mirrors placed 10cm apart in a Invar metal enclosure. One mirror is attached to a PZT, which allows for adjustment of the cavity frequency. The temporal mode of transmitted photons is determined by the cavity bandwidth following Equation (3.36), and using such a narrowband cavity essentially elongates the photons in time. The addition of this new cavity is shown Figure 4.5, along with the optionally-connected section of Figure 3.3. For simplicity, we are initially only looking at single photons with this new setup rather than attempting to generate qubits.

The use of such a narrowband cavity introduces several challenges into the experiment which must be addressed. First, the total count rate is drastically reduced as a result of the stricter filtering. This causes data acquisition to be much slower, and special care must be taken to ensure that neither the cavity frequency nor the laser frequency drifts during an experimental run. Dark counts also become more relevant, although they are still fewer than

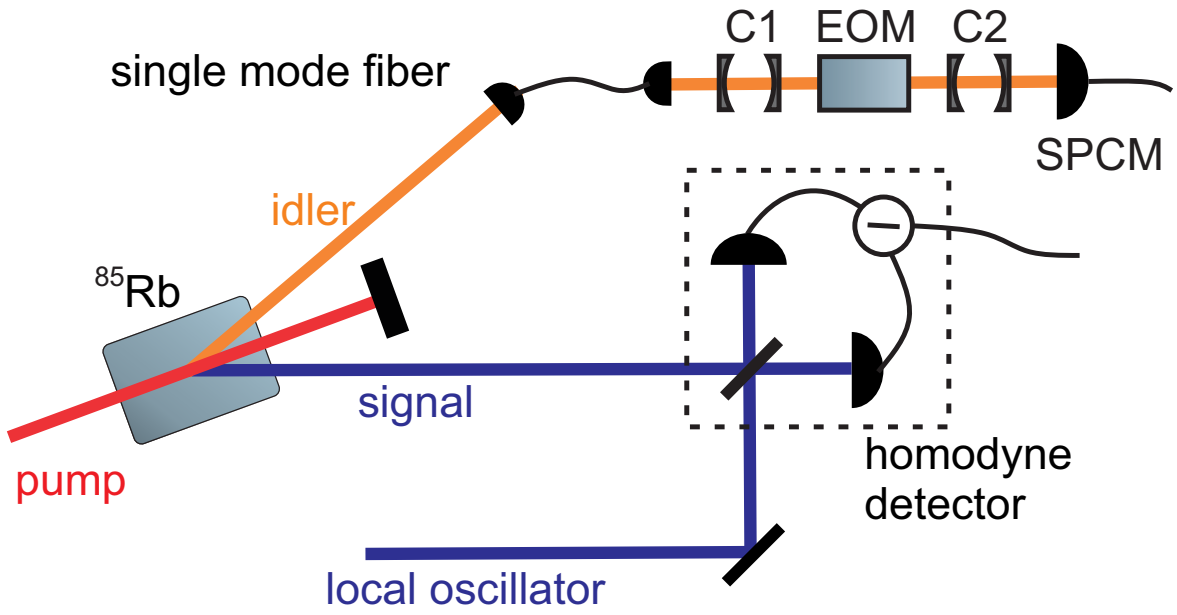

Figure 4.5: Experimental design including narrowband cavity and optional EOM. C1 is the 55 MHz bandwidth monolithic lens cavity used in all experiments up to this point. C2 is a 7 MHz bandwidth Fabry-Pérot cavity introduced to extend the temporal mode.

the idler counts by about an order of magnitude. Furthermore, the real-time monitoring of the variance shown in Figure 3.5 is no longer an effective tool for experiment alignment, as the required statistics are acquired too slowly and the photon is spread out much more thinly over a large range of time bins. This required the development of a way to switch between not having the narrowband cavity in place for experimental alignment and having it in place for data acquisition. We accomplished this by switching the fiber connections in the idler channel around after the lens cavity. The fiber could be directly inserted into the SPCM for alignment, and then efficiently moved to the narrowband cavity path.

The relative frequency drift between the laser and the cavity was an issue that had to be addressed in order to acquire a large data set under the same conditions. Locking the frequency of the narrowband cavity to reduce drift was appealing, however due to the very low count rate even a small amount of leaked light from the locking beam would completely overwhelm the idler count rate. Due to this, we decided a lock was not the way to go and an-

other system had to be developed. We accomplished this by sending a strong, classical beam along the idler channel using the conveniently already-existing seed beam. We were able to monitor and correct the frequency drift of the narrowband cavity by measuring the transmission of this classical beam and correcting it using the cavity PZT. Computer-controlled shutters were placed before the seed beam combines with the idler path and immediately before the SPCM. This allows us to automatically block this beam when taking data with the SPCM, and then unblock the beam when not taking data to ensure the frequency of the cavity has not drifted. Large data sets are accumulated at identical conditions by taking a series of small data sets and switching back and forth in this way.

As the narrowband cavity extended the signal temporal mode in time, determining the temporal mode accurately became much more significant for achieving high efficiency reconstruction of the state. A guessed sum of Gaussians was no longer adequate, and the autocorrelation method introduced in Section 3.5 and fully described in Appendix A was necessary to faithfully determine the temporal mode. The main idea stems from Equation (A.7), which relates the autocorrelation matrix $\hat{A} = \langle i(t_i)i(t_j)\rangle$ to the density matrix in the time-bin basis. The autocorrelation matrix in the triggered case when the signal is present is calculated, and then the autocorrelation matrix for random triggered background is subtracted from that. This leaves only the contribution from the signal to the density matrix in the time-bin basis remaining. We can represent this as:

$$\hat{\rho}_{temporal} = \sum_i P_i |\psi\rangle\langle\psi| \tag{4.5}$$

If the signal state is in a pure temporal mode, this matrix should only have one single eigenvector which we can write as:

$$|\psi\rangle = \sum_j \phi(t_j)|1_j\rangle \tag{4.6}$$

where the sum exists over all of the time bins of our digital acquisition card. $\phi(t)$ can be recognized as the temporal mode and $|1_j\rangle$ represents a single photon being present in the j^{th} time bin.

Experimentally, the autocorrelation matrix comes directly from the HD photocurrent and thus is straightforward to find. Once the background contributions are subtracted, this matrix can be diagonalized and the primary eigenvalue determined. The eigenvector corresponding to this eigenvalue gives the temporal mode from Equation (4.6). More complex situations, such as the existence of any detuning between the LO and the corresponding conjugate cavity frequency, or finite HD response are discussed in Appendix A.

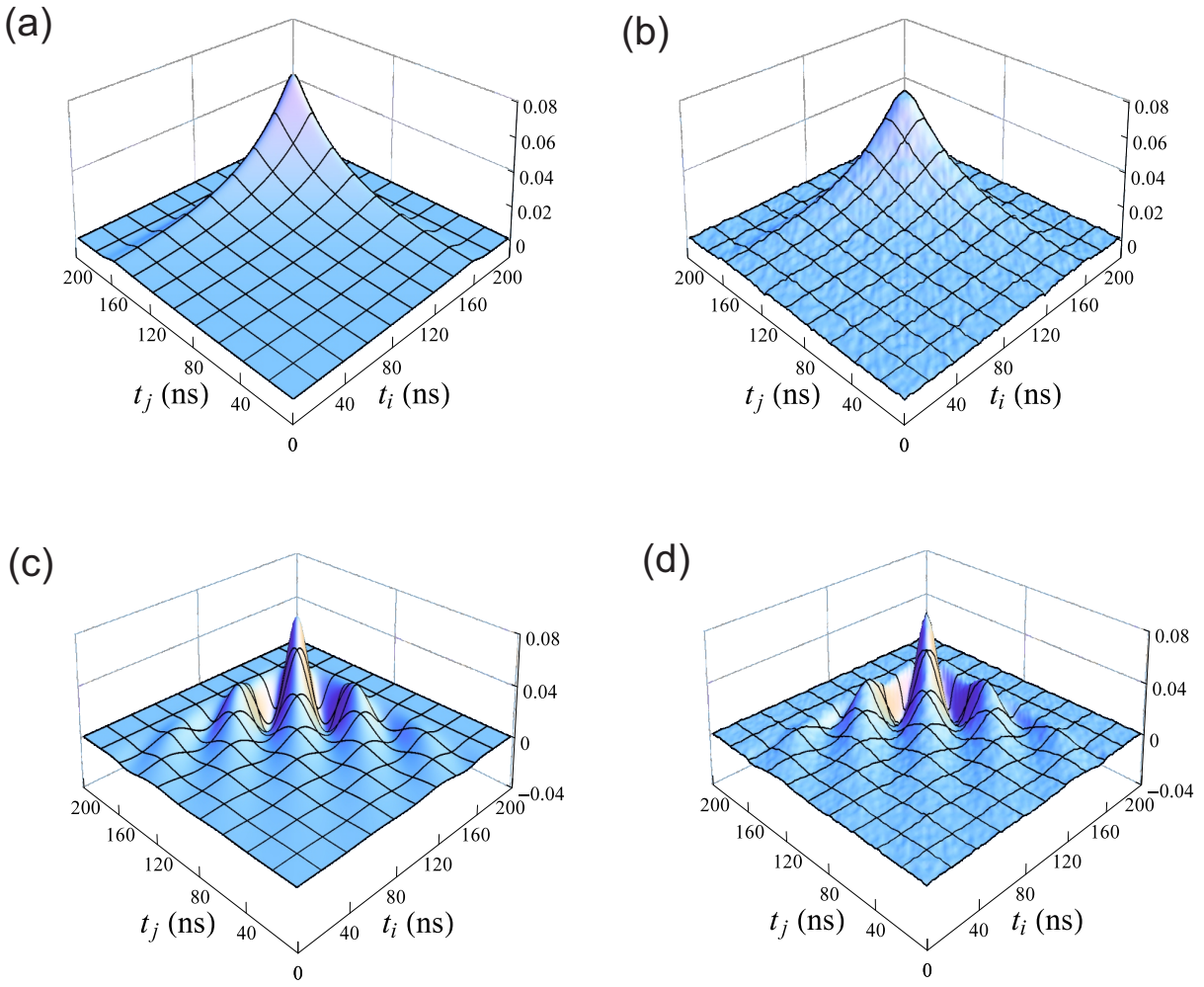

Figure 4.6: Theoretical and experimental autocorrelation matrices using the narrowband cavity to extend the temporal mode. (a) The predicted autocorrelation matrix with no detuning between the cavity and $2\omega_p - \omega_{LO}$. (b) Experimental results for the no-detuning case. (c) Theoretical prediction corresponding to a 16.8 MHz detuning. (d) Experimental results for 16.8 MHz detuning.

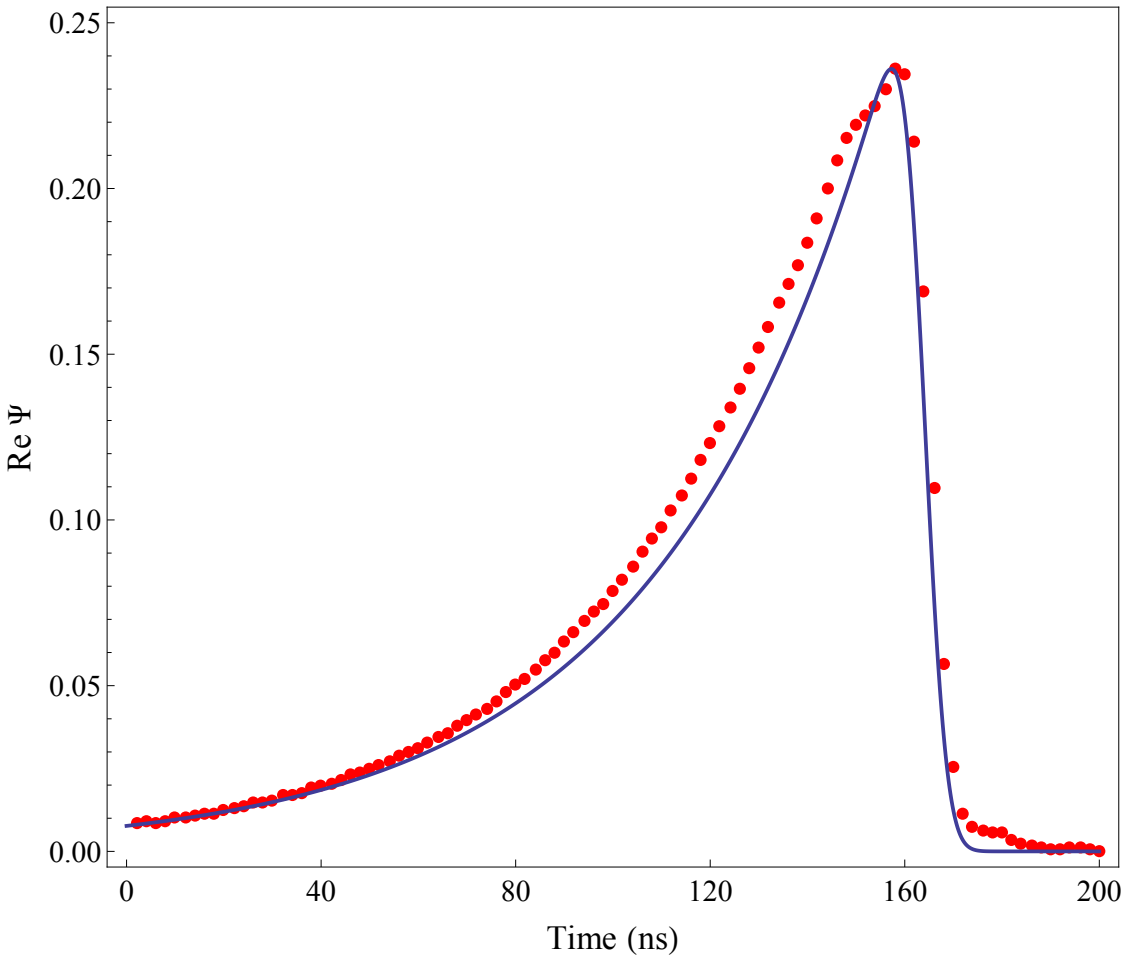

Figure 4.7: Inferred temporal mode with the presence of the narrowband cavity. This was determined by diagonalizing the autocorrelation matrix and finding the primary eigenvector. The profile closely follows the predicted one-sided exponential as discussed in Section 3.5.

From our experimental data, this technique shows very good results with the narrowband cavity setup. Figure 4.6 plots a comparison between predicted and experimental autocorrelation matrices, with and without detuning between the LO and corresponding conjugate cavity frequency. Using Equation (A.7), we can correct for the effect of a detuning of the signal carrier frequency from the LO, and then diagonalize the remaining temporal density matrices. The primary eigenvectors are found, which gives the temporal mode of the signal. Figure 4.7 shows the inferred signal temporal mode from a series of measurements including 8 different detunings with 200000 trigger events each. The result very closely matches the predicted single-sided exponential predicted in Section 3.5.

Once the temporal mode has been obtained, reconstruction of the density matrix follows the same techniques as described in Sections 2.4.3 and 2.5. This results in first the quadrature and then the most probable density matrix that matches the data. These results are shown in the following density matrix:

$$\hat{\rho} = \begin{pmatrix} 0.463 & 0 & 0 & 0 \\ 0 & 0.525 & 0 & 0 \\ 0 & 0 & 0.012 & 0 \\ 0 & 0 & 0 & 7 \cdot 10^{-5} \end{pmatrix} \tag{4.7}$$

Figure 4.8 shows the reconstructed quadrature distribution. Interestingly, the resulting density matrix has a higher single photon component ($\rho_{11} = 0.525$) than previous results without the narrowband cavity. This is quite impressive considering SPCM dark counts are much more significant in the narrowband cavity case, which would serve to decrease ρ_{11}. Furthermore, the two-photon component ρ is also much lower at $\rho_{22} = 0.012$, compared to without the narrowband cavity where typically $\rho_{22} = 0.06$. This indicates that the limited HD bandwidth and its corresponding effect on our ability to measure and reconstruct the temporal mode plays a significant role in our measurements without the narrowband cavity.

One of interesting ideas that has developed out of this experiment is the idea that we should be able to reconstruct a completely arbitrary and unknown incoming signal using this autocorrelation technique. In particular, we aim to use this technique to determine the temporal mode of a state with multiple, unknown frequency components. To test this idea, we have implemented an electro-optic modulator (EOM) in the idler channel before the narrowband cavity. The EOM is set up in the phase-modulation configuration, which corresponds to the creation of frequency sidebands that would make it through the cavity to the SPCM. This will project the signal onto the same frequency mode including sidebands, as determined by the transmission of the idler mode. Some theory on how this will affect the autocorrelation function has been discussed in Section A.3. This addition to the experiment is new and still in progress at the moment. We have been able to generate 20 MHz sidebands

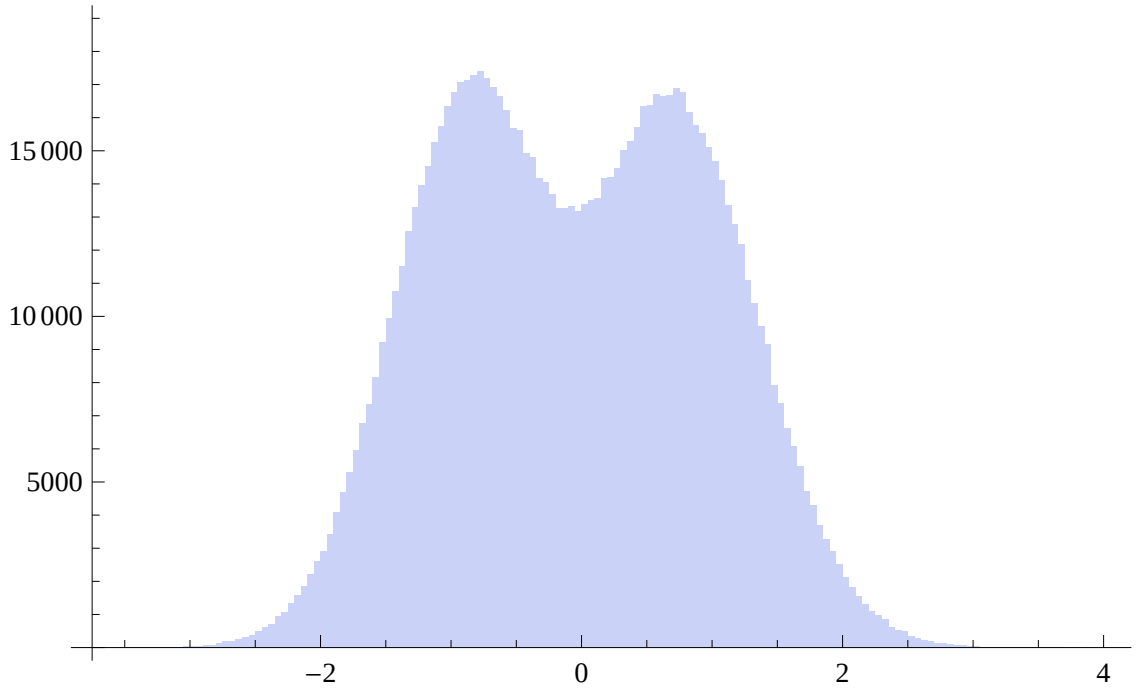

Figure 4.8: Reconstructed quadrature distribution using the narrowband cavity. The clear dip around the origin shows a strong single photon component.

and measure the autocorrelation matrix, shown in Figure 4.9. Unfortunately, since the arrival of photon events is random in time, the phase of the EOM modulation is also random from event to event. This effectively creates a phase-randomized mixture of temporal modes which cannot be described by a pure temporal mode. A derivation of this effect is given in Appendix A.3.

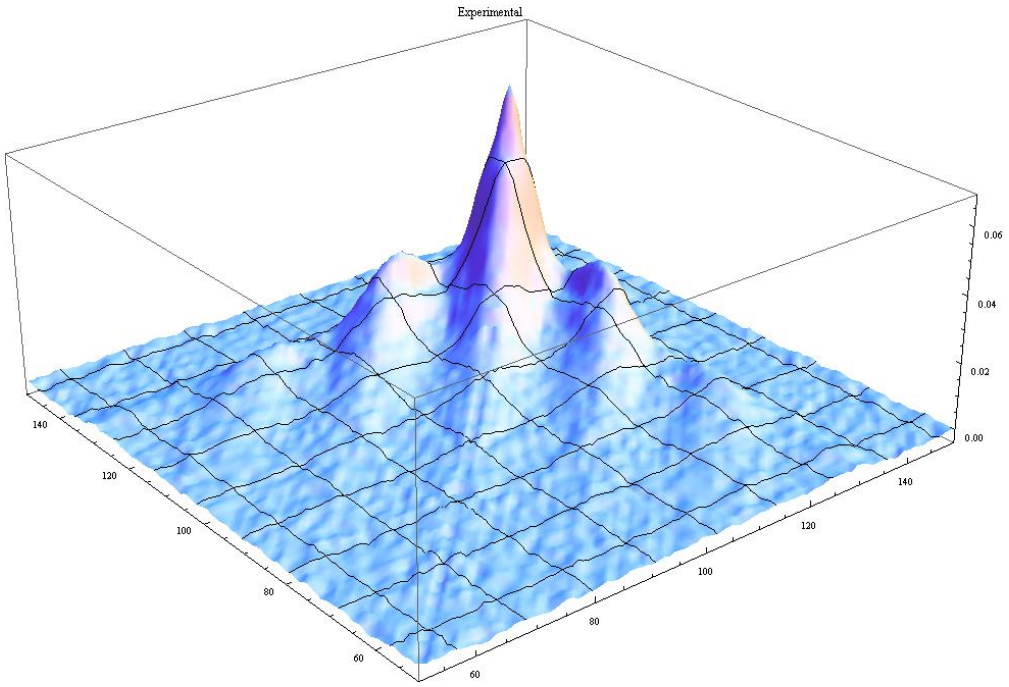

Figure 4.9: Autocorrelation matrix using an EOM to generate frequency sidebands.

Chapter 5

Extension to Atomic Quantum States

5.1 DLCZ Protocol

So far, most of this thesis has focused on using the FWM process to generate quantum states in the optical domain. In the previous chapter, we described how an arbitrary single-mode superposition state could be prepared by using conditional measurements on one mode of an optical two-mode squeezed state (TMSS). We have shown how FWM in atomic ensembles can compete with the established techniques of SPDC. However, using atomic ensembles opens up exciting new possibilities, in that with some clever manipulation, the collective atomic states themselves can be manipulated and then later measured, something that is not accessible using SPDC.

Following the protocol introduced by Duan, Lukin, Cirac, and Zoller [11], the Stokes and anti-Stokes transitions involved in FWM can be separated in time. This allows for brief storage of one mode of the TMSS as a collective excitation of the atomic ensemble followed by optical readout of the state. Originally proposed as a technique for implementing quantum repeaters and long distance quantum communications, the DLCZ protocol also has garnered much interest for its ability to store a heralded atomic excitation and then achieve on-demand readout. Previous experiments have already demonstrated stored heralded single atomic excitations [33, 34, 70, 71]. However, the DLCZ protocol is not limited to single photons and can be extended to generate arbitrary collective atomic state. Our previously described results in generating optical qubits can be understood as the transient generation of a collective atomic qubit state followed by its immediate optical readout. While this interpretation takes a bit of argument to make, we aim to extend this work to time-separated write and read stages using the DLCZ protocol, and present in this chapter an outline of the

procedure.

The basic idea of DLCZ is shown in Figure 5.1. An ensemble of N three-level atoms in the Λ configuration is considered, with metastable states $|g\rangle$, $|e\rangle$ and an intermediate excited state $|i\rangle$. The atoms are prepared in the collective ground state $|\psi_0\rangle = |g_1 g_2 \dots g_N\rangle$. In our experiment, this collective ground state is achieved using optical pumping. A weak, off-resonant "write" pulse is then sent through the sample. This write pulse initiates a Raman scattering event $|g\rangle \rightarrow |i\rangle \rightarrow |e\rangle$ with some probability, which is then spectrally filtered and detected by a SPCM within a narrow solid angle. By conditioning on a detection event, this heralds that one of the atoms has transitioned to the excited state $|e\rangle$. Assuming that the detector is placed much further away from the atomic ensemble than the size of the ensemble, scattered photons from opposite sides of the cloud are detected within a sufficiently small angle such that good interference visibility is always achieved. Thus, information about which atom was excited is fundamentally indistinguishable, resulting in the superposition of all possible permutations of a single excitation. This state, known as a collective spin excitation (CSE), can be written after the write event as follows:

$$|\psi_w\rangle = \frac{1}{\sqrt{N}} \sum_{n=1}^{N} e^{i\phi_n} |g_1 g_2 \dots e_n \dots g_N\rangle \tag{5.1}$$

where the phase terms ϕ_n represent the momentum kick associated with the scattering. This excitation can be described in terms of the collective raising operator:

$$|\psi_w\rangle = \hat{S}^\dagger |g_1 g_2 \dots g_N\rangle \tag{5.2}$$

where $\hat{S}^\dagger \equiv (1/\sqrt{N}) \sum_n \hat{S}_n^\dagger$ with $\hat{S}_n^\dagger = |e_n\rangle\langle g_n| e^{i\phi_n}$ representing the individual atomic raising operator.

The resulting state is now prepared for readout. This is accomplished via a strong on-resonant "read" pulse. This converts the collective atomic excitation back to an optical state coherently through the $|e\rangle \rightarrow |i\rangle \rightarrow |g\rangle$ Raman transition. This optical signal photon can then be measured and characterized using existing well-developed optical techniques. The

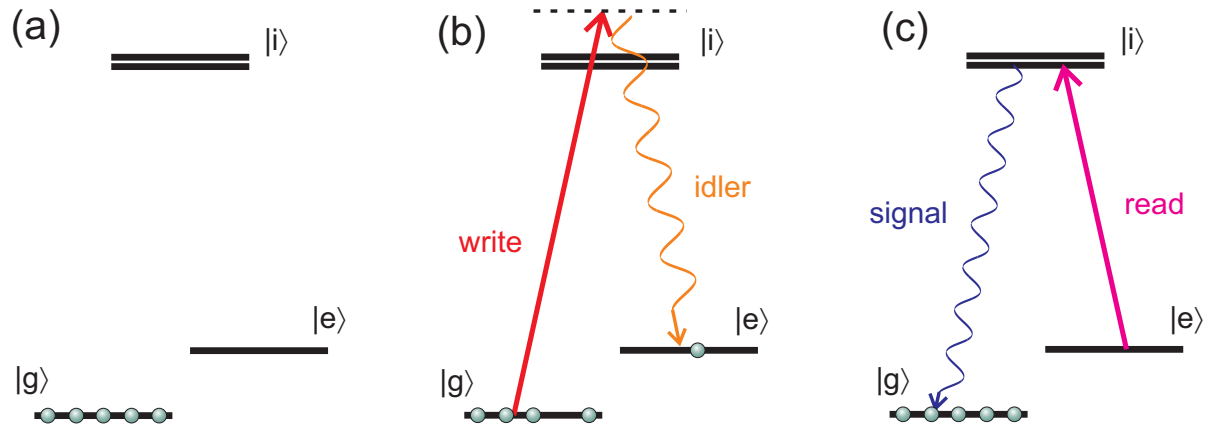

Figure 5.1: DLCZ protocol. (a) An ensemble of atoms are prepared in the collective ground state $|g_1 g_2 \ldots g_N\rangle$ of a three-level Λ system. (b) An off-resonant write pulse scatters an idler photon as a single excitation to $|e\rangle$ occurs collectively across the atoms. A SPCM heralds the occurrence of this event. (c) After some storage time, a strong on-resonant read pulse efficiently transfers the atomic state to an optical signal state along the phase matched direction.

read transition is strongly enhanced along the phase matched k-vector by an interference effect known as *collective enhancement*, which is crucial to the DLCZ process and is discussed thoroughly in the next section. The end result is a cyclic transition, where the atoms return to their original collective ground state, and a pair of entangled signal and idler photons are emitted similarly to FWM.

5.2 Collective Enhancement

The success of the DLCZ protocol hinges on an interference effect known as collective enhancement. After the measurement of the write photon, the atomic state is prepared in a collective superposition where each atom has a probability of being in the excited state. Fortunately, the phase acquired by each possible excitation of an atom causes constructive interference for the return transition to the collective ground state under phase matching conditions, leading to a strong enhancement of the read transition that scales with the num-

ber of atoms. This process is crucial in that it amplifies the probability that the read pulse will cause the signal photon to be generated, which amplifies the signal to noise ratio along the phase matched direction.

Upon detection of a single idler photon, we know the write transition has taken place. Recall that due to quantization of the electromagnetic field, $\vec{E}(\vec{r},t) \propto (\hat{a}_{\vec{k},s}(t)e^{i\vec{k}\cdot\vec{r}} + c.c.)$. Thus, the collective atomic ensemble has absorbed one pump photon and emitted one idler photon with k-vectors $\vec{k}_w$ and $\vec{k}_i$. This excites one atom from the ground state to the excited state, and since we cannot distinguish which one the result is the atomic superposition state with phases:

$$|\psi\rangle = \frac{1}{\sqrt{N}} \sum_{n=1}^{N} e^{i(\vec{k}_i - \vec{k}_w)\cdot\vec{r}_n} |g_1 g_2 \dots e_n \dots g_N\rangle \tag{5.3}$$

Next we consider what happens when the read pulse arrives. Unlike the write transition, we cannot simply herald upon a successful event and have to consider the case where the read pulse does not cause a Raman transition to the original ground state. Let us assume that due to the read pulse each atom has a probability g^2 to undergo the Raman transition from $|e\rangle$ to $|g\rangle$. The two-mode state corresponding to $|\text{atomic state}\rangle \otimes |\text{signal photon}\rangle$ after the read pulse becomes:

$$|\Psi\rangle = \frac{\sum_{n=1}^{N} e^{i(\vec{k}_i - \vec{k}_w)\cdot\vec{r}_n} |g_1 g_2 \dots e_n \dots g_N\rangle \otimes |0\rangle + g \sum_{n=1}^{N} e^{i\Delta\vec{k}\cdot\vec{r}_n} |g_1 g_2 \dots g_N\rangle \otimes |1\rangle}{\sqrt{N + \left| g \sum_{n=1}^{N} e^{i\Delta\vec{k}\cdot\vec{r}_n} \right|^2}} \tag{5.4}$$

where $\Delta\vec{k} \equiv (\vec{k}_i + \vec{k}_s - \vec{k}_w - \vec{k}_r)$. For large N, we can make the simplification that $\sum_{n=1}^{N} e^{i\Delta\vec{k}\cdot\vec{r}_n} = N\delta^3(\Delta\vec{k})$. Along the phase matched angle where $\Delta\vec{k} = 0$, we see that collective enhancement

of the read transition occurs, with the final two-mode density matrix becoming:

$$\begin{aligned}\rho &= \frac{\sum_{n,m=1}^{N} \rho_{nm} + g^2N^2\rho_{read}}{N + g^2N^2} \\ &= \frac{1}{1+1/(g^2N)}\rho_{read} + \frac{1}{N+g^2N^2}\sum_{n,m=1}^{N}\rho_{nm} \\ &\approx \Big(1 - \frac{1}{g^2N}\Big)\rho_{read} + \frac{1}{N+g^2N^2}\sum_{n,m=1}^{N}\rho_{nm}\end{aligned} \tag{5.5}$$

here, ρ_{read} represents a successful read transition, while each of the components of the sum $\rho_{nm} = e^{i(\vec{k}_i - \vec{k}_w)\cdot\vec{r}_n - i(\vec{k}_i-\vec{k}_w)\cdot\vec{r}_m}|g_1g_2\ldots e_n\ldots g_N, 0\rangle\langle g_1g_2\ldots e_m\ldots g_N, 0|$ corresponds to individual density matrix elements of a failed read transition that left the atomic state still excited. For typical experiments, $N \approx 10^{13}$, leading to effectively perfect readout of the state (at least, assuming no decoherence).

Another concern for successful readout is that the state does not decay due to spontaneous emission prior to a read event. This concern is addressed thoroughly in the supplementary information of the DLCZ paper [11] by considering a low finesse cavity aligned along the signal channel with the read beam present. The rate of emission into the cavity κ' gives the rate of successful read events, while spontaneous decay rate γ_s' out of the cavity gives the rate of losses due to spontaneous emission. By then taking the limit that the cavity finesse approaches one, the model approaches the no-cavity limit. The resulting signal to noise ratio, defined by the $R \equiv \kappa'/\gamma_s'$ is then found to be:

$$R = \frac{4N_aL_a|g_c|^2}{c\gamma_s} \approx d_0 \tag{5.6}$$

where N_a is the total number of atoms, L_a is the length of the interaction, g_c is the atom-cavity coupling, and d_0 is the on-resonant optical depth. Thus, the signal to noise ratio along the signal channel is also collectively enhanced by the number of atoms. From these results, we can see that for the large number of atoms present in a typical DLCZ experiment, collective enhancement allows for nearly-deterministic readout of the state with a high signal to noise ratio along the phase matched direction.

5.3 Applying Conditional Measurements to the FWM Process

The description of the CSE mode up to this point has considered a single CSE excitation, however similar to any oscillator higher order excitations can be exist and can be utilized as well. Assuming a sufficiently strong pump such that depletion can be neglected, the dynamics of the write event can be described by the Hamiltonian [11]:

$$\hat{H} = \hbar(\gamma \hat{S}^\dagger \hat{a}_i^\dagger + \gamma^* \hat{S} \hat{a}_i) \tag{5.7}$$

where $\hat{a}_i$ is the photonic annihilation operator for the idler mode and $\hat{S}$ is the CSE annihilation operator described in Equation (5.2). This Hamiltonian is identical to the two-mode squeezing Hamiltonian (3.19) that we encountered with two optical modes for FWM, however in this case one of the modes is the atomic CSE mode. By applying the two-mode squeezing operator associated with this Hamiltonian to the vacuum state similar to Equation (3.28), we end up with the following state in the two-mode basis $|\text{CSE excitations}\rangle \otimes |\text{idler photons}\rangle$:

$$\begin{aligned} |\Psi\rangle &= \frac{1}{\cosh(|\gamma t|)} \sum_{n=0}^{\infty} (-e^{(i \arg(-i\gamma t))} \tanh(|\gamma t|))^n |n, n\rangle \\ &\approx |0,0\rangle - i\gamma t |1,1\rangle - \gamma^2 t^2 |2,2\rangle + ... \end{aligned} \tag{5.8}$$

We can now perform the same projective measurement technique as described in Section 4.1 upon the idler mode. By combining the idler with a weak coherent beam and heralding upon detection of an exact number of photons, the CSE state is projected onto a superposition state whose components depend on the amplitude and phase of the coherent beam. As was the case for photons, this can be extended to generate arbitrary CSE superposition states up to N excitations, by using N coherent beams and N single photon detectors. This arbitrary CSE state can then be efficiently mapped onto the optical signal mode due to the collective enhancement process described in Section 5.2 and measured using optical detection techniques such as homodyne detection. The experimental results for generating optical qubits shown in Section 4.2 can be interpreted as precisely this process, only with transient

CSE state generation and immediate optical readout. However, this represents a first step towards complete control over the atomic CSE state Hilbert space.

Chapter 6

Conclusion

In this thesis, I have described our experimental work in developing a four-wave mixing (FWM) system as a source of nonclassical states. Present measurements have demonstrated the generation of single photons and arbitrary qubits in the optical domain with generalized efficiencies in the 40-50% range, while retaining the high spectral brightness that is characteristic of the FWM process. While the generation of highly efficient qubits has been demonstrated before, their creation from FWM at the efficiencies and count rates that we have achieved is novel. One of the main advantages of the FWM process in atoms is that it allows access to not only optical states but also to collective spin excitations (CSEs) in atoms. At present, the CSE qubit exists only transiently, but by moving to a pulsed excitation regime akin to the DLCZ protocol [11] this system allows for the creation and manipulation of longer lived CSEs. One of the primary future goals of this experiment is to ultimately demonstrate the heralded generation of arbitrary CSE qubit states. By preparing and characterizing arbitrary optical qubits from FWM, we have demonstrated the quantum state engineering side of this task and taken a step in that direction.

One of the important developments in this thesis is the creation of a model which takes into account experimental imperfections, as was described in Section 4.3. This has allowed us to not only model the FWM process including higher photon number states but also to integrate the effects of optical losses, spatial and temporal mode mismatch, limited homodyne detector bandwidth, and background thermal noise. While none of these effects explain the reduced coherence observed in our experimental results, the creation of this model has allowed us to rule them out as the cause of this effect. The current conjecture for the source of this decoherence is some residual distinguishability between photons coming from our coherent

source and the FWM process. Further investigation is required to determine the exact source of this distinguishability.

Several steps could be taken to improve the experimental apparatus. The limited bandwidth of the homodyne detector results in distortion of the measured temporal mode, causing a mode mismatch upon reconstruction. Similar to spatial mode mismatch, this manifests itself as loss due to imperfect visibility [49]. Using a faster homodyne detector which has a much larger bandwidth than the bandwidth of the signal photons would allow us to neglect the response function of the detector, allowing for an elimination of this loss. Alternatively, a narrower filter cavity could be used in the idler channel to reduce the bandwidth of the signal photons, however this comes at the expense of reduced count rate and stability. The integration of such a narrowband cavity into the experiment is currently in progress. Preliminary results show promise and have been described in Section 4.4. We have also developed a technique which allows us to determine the temporal mode experimentally, as described in Section 4.4 and Appendix A, which should serve as a useful tool to ensure high efficiency temporal mode matching.

The ability to create arbitrary quantum states has tremendous applications across the field of quantum information science. The simultaneous demonstration of relatively high efficiency and high spectral brightness from FWM show that it has the potential to compete with SPDC as a nonclassical light source. Since in FWM the photon pairs are generated from an atomic source, they are conveniently close to atomic transitions and have compatible bandwidths. This could be useful for atom-based quantum devices such as memories and repeaters. Furthermore, the ability of this FWM process to generate arbitrary collective atomic states could prove useful in preparing the internal states of these devices directly without having to send in an nonclassical input signal, which can be inefficient. These collective atomic states also present a novel system whose potential has not been thoroughly explored, mainly due to the past difficultly of manipulating them. Four-wave mixing thus

presents an exciting avenue for progress in both practical technologies and fundamental research, and I look forward to what it will bring in the future.

Appendix A

Derivation of Autocorrelation Matrix Relations

A.1 Relation of Autocorrelation to Density Matrix

In this section we seek to find the temporal mode of the signal state from the homodyne photocurrent $i(t)$. Given that our acquisition card is digital, the photocurrent data is saved in discrete time bins, denoted i_j for the j^{th} time bin. Using the autocorrelation matrix with elements $A_{jk} = \langle i_j i_k \rangle$, we relate this to the density matrix in the time-bin basis as defined below. Here, the expectation value is taken over all experimental data points.

Consider a single photon which is in a single time bin t_j with probability ρ_{jj}. We denote the state of this photon being in the j^{th} bin as $|j\rangle$, where:

$$|j\rangle = \hat{a}_j^\dagger|0\rangle = \hat{a}_j^\dagger|0\rangle_1 \ldots |0\rangle_{j-1}|0\rangle_j|0\rangle_{j+1}\cdots = \ldots|0\rangle_{j-1}(\sqrt{1}|1\rangle_j)|0\rangle_{j+1}\ldots \tag{A.1}$$

where indices indicate the different time bins. For convenience, we write the state of having no photons in any bin as $|0\rangle$ and the having two photons in the j^{th} bin as $|2_j\rangle$. A photon in a pure temporal mode which is distributed over many bins can described by the state $|\psi\rangle = \sum_j \phi(t_j)|j\rangle$, where $\phi(t)$ is the temporal mode. For mixed states, the time-bin basis density matrix is introduced as:

$$\hat{\rho} = \sum_n P_n|\psi_n\rangle\langle\psi_n| \tag{A.2}$$

It is important to emphasize that this is not the usual Fock-basis density matrix. Instead of the photon-number information, here we seek to find information about the time-bin distribution - the temporal mode. If the signal is a pure temporal mode, then diagonalizing this time-bin density matrix and taking its primary eigenvector yields the single temporal mode vector $|\psi\rangle$.

To find this, we can write the quadrature operators for a single time bin in terms of the annihilation and creation operators:

$$\hat{X}_j = \frac{\hat{a}_j + \hat{a}_j^\dagger}{\sqrt{2}} \tag{A.3}$$

Assuming perfection detector resolution we find:

$$\begin{aligned} A_{jk} &= \langle i_j i_k \rangle \\ &\propto \langle \hat{X}_j \hat{X}_k \rangle \\ &= \mathrm{Tr}\left[\sum_{m,n} \rho_{mn} |m\rangle\langle n| \hat{X}_j \hat{X}_k\right] \\ &= \sum_{m,n,l} \rho_{mn} \langle l|m\rangle \langle n|\hat{X}_j \hat{X}_k|l\rangle \\ &= \sum_{m,n} \rho_{mn} \langle n|\hat{X}_j \hat{X}_k|m\rangle \end{aligned} \tag{A.4}$$

We now need to compute the term $\langle n|\hat{X}_j\hat{X}_k|m\rangle$. Furthermore, we can also consider the situation where our signal field is detuned by Δ from our phase reference (for homodyne tomography, this would be the phase of our local oscilllator). In this case, the operators evolve in time according to $\hat{a}(t) = \hat{a}(0)e^{-i\Delta t}$, $\hat{a}^\dagger(t) = \hat{a}^\dagger(0)e^{i\Delta t}$. Expanding out the quadrature operators we then get:

$$\begin{aligned} \langle n|\hat{X}_j\hat{X}_k|m\rangle &= \frac{1}{\sqrt{2}}\langle n|\hat{X}_j\left[e^{-i\Delta t_m}\delta_{km}|0\rangle + \sqrt{2}e^{i\Delta t_m}\delta_{km}|2_m\rangle + e^{i\Delta t_k}(1-\delta_{km})|jm\rangle\right] \\ &= \frac{1}{2}\langle n|\Big[e^{-i\Delta(t_m-t_j)}\delta_{km}|j\rangle + 2\delta_{jm}\delta_{km}|m\rangle + (1-\delta_{km})(\delta_{jk}|m\rangle + e^{-i\Delta(t_m-t_k)}\delta_{jm}|k\rangle)\Big] \\ &= \frac{1}{2}\Big[e^{-i\Delta(t_m-t_j)}\delta_{km}\delta_{nj} + 2\delta_{jm}\delta_{km}\delta_{nm} + (1-\delta_{km})(\delta_{jk}\delta_{nm} + e^{-i\Delta(t_m-t_k)}\delta_{jm}\delta_{nk})\Big] \end{aligned} \tag{A.5}$$

We can now compute the sum (A.4):

$$
\begin{aligned}
A_{jk} &\propto \sum_{m,n} \rho_{mn} \langle n|\hat{X}_j \hat{X}_k|m\rangle \\
&= \frac{1}{2}\sum_{m,n} \rho_{mn}\Big[e^{-i\Delta(t_m-t_j)}\delta_{km}\delta_{nj} + 2\delta_{jm}\delta_{km}\delta_{nm} + (1-\delta_{km})(\delta_{jk}\delta_{nm} + e^{-i\Delta(t_m-t_k)}\delta_{jm}\delta_{nk})\Big] \\
&= \frac{1}{2}\sum_{n}\Big[e^{-i\Delta(t_k-t_j)}\delta_{nj}\rho_{kn} + 2\delta_{jk}\delta_{nk}\rho_{kn} + \delta_{jk}\rho_{nn} \\
&\qquad + e^{-i\Delta(t_j-t_k)}\delta_{nk}\rho_{jn} - \delta_{jk}\delta_{nk}\rho_{kn} - e^{-i\Delta(t_k-t_k)}\delta_{jk}\delta_{nk}\rho_{kn}\Big] \\
&= \frac{1}{2}\Big[e^{-i\Delta(t_k-t_j)}\rho_{kj} + 2\delta_{jk}\rho_{kk} + \delta_{jk}\mathrm{Tr}[\hat{\rho}] + e^{-i\Delta(t_j-t_k)}\rho_{jk} - \delta_{jk}\rho_{kk} - \delta_{jk}\rho_{kk}\Big] \\
&= \frac{e^{-i\Delta(t_j-t_k)}\rho_{jk} + e^{i\Delta(t_j-t_k)}\rho_{kj}}{2} + \frac{1}{2}\delta_{jk} \\
&= \mathrm{Re}(\rho_{jk})\cos(\Delta(t_j-t_k)) + \mathrm{Im}(\rho_{jk})\sin(\Delta(t_j-t_k)) + \frac{1}{2}\delta_{jk}
\end{aligned}
\tag{A.6}
$$

where the last step uses the fact that $\hat{\rho}$ is self-adjoint. Then

$$
\hat{A} \propto \mathrm{Re}(\hat{\rho})\cos(\Delta(t_j-t_k)) + \mathrm{Im}(\hat{\rho})\sin(\Delta(t_j-t_k)) + \frac{1}{2}\mathbb{1} \tag{A.7}
$$

with the constant of proportionality given by $2g^2|\alpha|^2$ where g is the HD gain. By taking measurements over a range of LO frequencies corresponding to various detunings Δ, the real and imaginary parts of $\hat{\rho}$ can be directly determined from the autocorrelation matrix.

A.2 Consideration of Homodyne Detector Bandwidth

The previous derivation was made under the assumption that the homodyne detector has an instantaneous response function, and then $i(t) = A\alpha X_\theta(t)$. However, for a real detector there is the introduction of electronic noise i_e and a non-instantaneous response function $r(t-t')$. This affects the photocurrent, which follows the expression $i(t) = A\alpha \int X_\theta(t')r(t-t')dt' + i_e(t)$

in the realistic case. The autocorrelation matrix relation then follows:

$$\begin{aligned}
A_{jk} &= \langle i(t_j)i(t_k)\rangle \\
&= A^2\alpha^2\Big\langle \iint_{-\infty}^{\infty} X_{\theta_{t'}}(t')r(t_j-t')X_{\theta_{t''}}(t'')r(t_k-t'')dt'dt''\Big\rangle + \langle i_e(t_j)i_e(t_k)\rangle \\
&= A^2\alpha^2 \iint_{-\infty}^{\infty} \langle X_{\theta_{t'}}(t')X_{\theta_{t''}}(t'')\rangle r(t_j-t')r(t_k-t'')dt'dt'' + \langle i_e(t_j)i_e(t_k)\rangle \\
&= A^2\alpha^2 \iint_{-\infty}^{\infty} \Big[\mathrm{Re}(\rho_{t',t''})\cos(\Delta(t'-t'')) + \mathrm{Im}(\rho_{t',t''})\sin(\Delta(t'-t'')) \\
&\qquad + \frac{1}{2}\delta_{t',t''}\Big] r(t_j-t')r(t_k-t'')dt'dt'' + \langle i_e(t_j)i_e(t_k)\rangle \\
&= \big\langle (i_{ideal} * r)(t_j)(i_{ideal} * r)(t_k)\big\rangle + \langle i_e(t_j)i_e(t_k)\rangle
\end{aligned} \tag{A.8}$$

From (A.8), we can see that the response function of the homodyne detector acts on the ideal autocorrelation matrix by 2D convolution (plus some background electronic noise). If the homodyne detector is fast enough, that is if its inverse bandwidth is much smaller than the temporal response function of the signal, this effect can be ignored. For a discussion of the losses that occur when the inverse HD bandwidth is comparable to the temporal response function of the signal, see [49].

A.3 Addition of EOM Sidebands

The result of Equation (A.7) is general, and holds for any time-bin density matrix $\hat{\rho}$. Experimentally, we aimed to generate a complex temporal mode by introducing phase modulation using an EOM. This modifies the temporal mode derived in Equation (3.36) to be the following:

$$|\psi\rangle = \sum_j e^{\gamma t_j/2} e^{i\beta\sin(\omega t_j+\phi)}\Theta(-t_j)|j\rangle \tag{A.9}$$

where β is the modulation strength, ω is the EOM frequency, and ϕ is the initial phase of the modulation.

Finding the density matrix elements yields:

$$\begin{aligned}\rho_{mn} &= \langle m|\psi\rangle\langle\psi|n\rangle \\ &= e^{\gamma(t_m+t_n)/2}\ e^{i\beta[\sin(\omega t_m+\phi)-\sin(\omega t_m+\phi)]}\Theta(-t_m)\Theta(-t_n) \\ &= e^{\gamma(t_m+t_n)/2}\ e^{2i\beta[\sin(\omega(t_m-t_n)/2)\cos(\omega(t_m+t_n)/2+\phi)]}\Theta(-t_m)\Theta(-t_n) \end{aligned} \tag{A.10}$$

This gives a nice density matrix with both real and imaginary parts that the autocorrelation technique should be able to experimentally measure. However, unfortunately in our experiment the timing of photon pair events was random, causing the phase ϕ to be completely randomized between trigger events. The result is that the signal state we actually measured the average over all possible ϕ, yielding:

$$\begin{aligned}\rho_{mn} &= \int_{-\pi}^{\pi} d\phi\ e^{\gamma(t_m+t_n)/2}\ e^{2i\beta[\sin(\omega(t_m-t_n)/2)\cos(\omega(t_m+t_n)/2+\phi)]}\Theta(-t_m)\Theta(-t_n) \\ &= e^{\gamma(t_m+t_n)/2}\cdot 2\pi J_o\Big(2\beta\sin\big(\frac{\omega}{2}(t_m-t_n)\big)\Big)\Theta(-t_m)\Theta(-t_n) \end{aligned} \tag{A.11}$$

where J_0 is a Bessel function. This density matrix unfortunately is strictly real. However, this model matches our experimentally measured density matrix with the EOM (Figure 4.9) very well. Modifying the experiment to either herald or postselect on a narrow range of ϕ would allow for the creation of the complex density matrix in Equation (A.10), at the cost of greatly reducing the count rate.

Bibliography

[1] A MacRae, T Brannan, R Achal, and AI Lvovsky. Tomography of a high-purity narrowband photon from a transient atomic collective excitation. *Physical Review Letters*, 109(3):033601, 2012.

[2] Travis Brannan, Zhongzhong Qin, Andrew MacRae, and AI Lvovsky. Generation and tomography of arbitrary qubit states in a transient collective atomic excitation. *arXiv preprint arXiv:1403.3463*, 2014.

[3] Alexander I Lvovsky and Michael G Raymer. Continuous-variable optical quantum-state tomography. *Reviews of Modern Physics*, 81(1):299, 2009.

[4] Albert Einstein, Boris Podolsky, and Nathan Rosen. Can quantum-mechanical description of physical reality be considered complete? *Physical Review*, 47(10):777, 1935.

[5] John S Bell et al. On the Einstein-Podolsky-Rosen paradox. *Physics*, 1(3):195–200, 1964.

[6] John F Clauser, Michael A Horne, Abner Shimony, and Richard A Holt. Proposed experiment to test local hidden-variable theories. *Physical Review Letters*, 23:880–884, 1969.

[7] Alain Aspect, Philippe Grangier, Gérard Roger, et al. Experimental realization of Einstein-Podolsky-Rosen-Bohm gedankenexperiment: a new violation of Bell's inequalities. *Physical Review Letters*, 49(2):91–94, 1982.

[8] CK Hong, ZY Ou, and Leonard Mandel. Measurement of subpicosecond time intervals between two photons by interference. *Physical Review Letters*, 59(18):2044–2046, 1987.

[9] R Hanbury Brown and RQ Twiss. Correlation between photons in two coherent beams of light. *Nature*, 177(4497):27–29, 1956.

[10] Nicolas Gisin, Grégoire Ribordy, Wolfgang Tittel, and Hugo Zbinden. Quantum cryptography. *Reviews of Modern Physics*, 74(1):145–195, 2002.

[11] L-M Duan, MD Lukin, J Ignacio Cirac, and Peter Zoller. Long-distance quantum communication with atomic ensembles and linear optics. *Nature*, 414(6862):413–418, 2001.

[12] Nicolas Sangouard, Christoph Simon, Hugues De Riedmatten, and Nicolas Gisin. Quantum repeaters based on atomic ensembles and linear optics. *Reviews of Modern Physics*, 83(1):33, 2011.

[13] DJ Wineland, JJ Bollinger, WM Itano, and DJ Heinzen. Squeezed atomic states and projection noise in spectroscopy. *Physical Review A*, 50(1):67, 1994.

[14] J Abadie, BP Abbott, R Abbott, TD Abbott, M Abernathy, C Adams, R Adhikari, C Affeldt, B Allen, GS Allen, et al. A gravitational wave observatory operating beyond the quantum shot-noise limit. *Nature Physics*, 7(12):962–965, 2011.

[15] Vittorio Giovannetti, Seth Lloyd, and Lorenzo Maccone. Quantum-enhanced measurements: beating the standard quantum limit. *Science*, 306(5700):1330–1336, 2004.

[16] Dik Bouwmeester, Jian-Wei Pan, Klaus Mattle, Manfred Eibl, Harald Weinfurter, and Anton Zeilinger. Experimental quantum teleportation. *Nature*, 390(6660):575–579, 1997.

[17] Juan Yin, Ji-Gang Ren, He Lu, Yuan Cao, Hai-Lin Yong, Yu-Ping Wu, Chang Liu, Sheng-Kai Liao, Fei Zhou, Yan Jiang, et al. Quantum teleportation and entanglement distribution over 100-kilometre free-space channels. *Nature*, 488(7410):185–188, 2012.

[18] Stephan Ritter, Christian Nölleke, Carolin Hahn, Andreas Reiserer, Andreas Neuzner, Manuel Uphoff, Martin Mücke, Eden Figueroa, Joerg Bochmann, and Gerhard

Rempe. An elementary quantum network of single atoms in optical cavities. *Nature*, 484(7393):195–200, 2012.

[19] Emanuel Knill, Raymond Laflamme, and Gerald J Milburn. A scheme for efficient quantum computation with linear optics. *Nature*, 409(6816):46–52, 2001.

[20] Erwan Bimbard, Nitin Jain, Andrew MacRae, and AI Lvovsky. Quantum-optical state engineering up to the two-photon level. *Nature Photonics*, 4(4):243–247, 2010.

[21] Max Hofheinz, H Wang, Markus Ansmann, Radoslaw C Bialczak, Erik Lucero, Matthew Neeley, AD O'Connell, Daniel Sank, J Wenner, John M Martinis, et al. Synthesizing arbitrary quantum states in a superconducting resonator. *Nature*, 459(7246):546–549, 2009.

[22] Dietrich Leibfried, Emanuel Knill, Signe Seidelin, Joe Britton, R Brad Blakestad, John Chiaverini, David B Hume, Wayne M Itano, John D Jost, Christopher Langer, et al. Creation of a six-atom Schrödinger catstate. *Nature*, 438(7068):639–642, 2005.

[23] Nicolas H Bonadeo, John Erland, D Gammon, D Park, DS Katzer, and DG Steel. Coherent optical control of the quantum state of a single quantum dot. *Science*, 282(5393):1473–1476, 1998.

[24] Alexander I Lvovsky, Barry C Sanders, and Wolfgang Tittel. Optical quantum memory. *Nature Photonics*, 3(12):706–714, 2009.

[25] L You and MS Chapman. Quantum entanglement using trapped atomic spins. *Physical Review A*, 62(5):052302, 2000.

[26] Sheng-wey Chiow, Tim Kovachy, Hui-Chun Chien, and Mark A Kasevich. $102\hbar k$ large area atom interferometers. *Physical Review Letters*, 107(13):130403, 2011.

[27] Paul G Kwiat, Klaus Mattle, Harald Weinfurter, Anton Zeilinger, Alexander V Sergienko, and Yanhua Shih. New high-intensity source of polarization-entangled photon pairs. *Physical Review Letters*, 75(24):4337, 1995.

[28] CK Hong and Leonard Mandel. Experimental realization of a localized one-photon state. *Physical Review Letters*, 56:58–60, 1986.

[29] Alexander I Lvovsky, Hauke Hansen, T Aichele, O Benson, J Mlynek, and S Schiller. Quantum state reconstruction of the single-photon fock state. *Physical Review Letters*, 87(5):050402, 2001.

[30] JS Neergaard-Nielsen, BM Nielsen, H Takahashi, AI Vistnes, and ES Polzik. High purity bright single photon source. *Optics Express*, 15(13):7940–7949, 2007.

[31] Han Zhang, Xian-Min Jin, Jian Yang, Han-Ning Dai, Sheng-Jun Yang, Tian-Ming Zhao, Jun Rui, Yu He, Xiao Jiang, Fan Yang, et al. Preparation and storage of frequency-uncorrelated entangled photons from cavity-enhanced spontaneous parametric down-conversion. *Nature Photonics*, 5(10):628–632, 2011.

[32] RE Slusher, LW Hollberg, Bernard Yurke, JC Mertz, and JF Valley. Observation of squeezed states generated by four-wave mixing in an optical cavity. *Physical Review Letters*, 55(22):2409, 1985.

[33] Caspar H van der Wal, Matthew D Eisaman, Axel André, Ronald L Walsworth, David F Phillips, Alexander S Zibrov, and Mikhail D Lukin. Atomic memory for correlated photon states. *Science*, 301(5630):196–200, 2003.

[34] A Kuzmich, WP Bowen, AD Boozer, A Boca, CW Chou, L-M Duan, and HJ Kimble. Generation of nonclassical photon pairs for scalable quantum communication with atomic ensembles. *Nature*, 423(6941):731–734, 2003.

[35] Shengwang Du, Pavel Kolchin, Chinmay Belthangady, GY Yin, and SE Harris. Subnatural linewidth biphotons with controllable temporal length. *Physical Review Letters*, 100(18):183603, 2008.

[36] James K Thompson, Jonathan Simon, Huanqian Loh, and Vladan Vuletić. A high-brightness source of narrowband, identical-photon pairs. *Science*, 313(5783):74–77, 2006.

[37] CF McCormick, Vincent Boyer, E Arimondo, and PD Lett. Strong relative intensity squeezing by four-wave mixing in rubidium vapor. *Optics Letters*, 32(2):178–180, 2007.

[38] Bharath Srivathsan, Gurpreet Kaur Gulati, Brenda Chng, Gleb Maslennikov, Dzmitry Matsukevich, and Christian Kurtsiefer. Narrow band source of transform-limited photon pairs via four-wave mixing in a cold atomic ensemble. *Physical Review Letters*, 111(12):123602, 2013.

[39] Max Planck. On the law of distribution of energy in the normal spectrum. *Annalen der Physik*, 4(553):1, 1901.

[40] Arthur H Compton. A quantum theory of the scattering of x-rays by light elements. *Physical Review*, 21(5):483, 1923.

[41] Willis E Lamb Jr and Marlan O Scully. The photoelectric effect without photons. Technical report, DTIC Document, 1968.

[42] Ulf Leonhardt. *Measuring the quantum state of light*, volume 22. Cambridge University Press, 1997.

[43] Howard Percy Robertson. The uncertainty principle. *Physical Review*, 34(1):163, 1929.

[44] Erwin Schrödinger. Der stetige übergang von der mikro-zur makromechanik. *Naturwissenschaften*, 14(28):664–666, 1926.

[45] Roy J Glauber. Coherent and incoherent states of the radiation field. *Physical Review*, 131(6):2766, 1963.

[46] Fortunato T Arecchi et al. Measurement of the statistical distribution of gaussian and laser sources. *Physical Review Letters*, 15(24):912–916, 1965.

[47] Eugene Wigner. On the quantum correction for thermodynamic equilibrium. *Physical Review*, 40(5):749, 1932.

[48] Frédéric Grosshans and Philippe Grangier. Effective quantum efficiency in the pulsed homodyne detection of a n-photon state. *The European Physical Journal D-Atomic, Molecular, Optical and Plasma Physics*, 14(1):119–125, 2001.

[49] Ranjeet Kumar, Erick Barrios, Andrew MacRae, AI Lvovsky, E Cairns, and EH Huntington. Versatile wideband balanced detector for quantum optical homodyne tomography. *Optics Communications*, 2012.

[50] Jaroslav Řeháček, Zdeněk Hradil, E Knill, and AI Lvovsky. Diluted maximum-likelihood algorithm for quantum tomography. *Physical Review A*, 75(4):042108, 2007.

[51] A. I. Lvovsky and M. G. Raymer. Continuous-variable optical quantum-state tomography. *Reviews of Modern Physics*, 81(1):299, 2009.

[52] Peter W Shor. Polynomial-time algorithms for prime factorization and discrete logarithms on a quantum computer. *SIAM Journal on Computing*, 26(5):1484–1509, 1997.

[53] Brian Julsgaard, Jacob Sherson, J Ignacio Cirac, Jaromir Fiurášek, and Eugene S Polzik. Experimental demonstration of quantum memory for light. *Nature*, 432(7016):482–486, 2004.

[54] Dominic W Berry, Alexander I Lvovsky, and Barry C Sanders. Interconvertibility of single-rail optical qubits. *Optics Letters*, 31(1):107–109, 2006.

[55] DW Berry and AI Lvovsky. Linear-optical processing cannot increase photon efficiency. *Physical Review Letters*, 105(20):203601, 2010.

[56] Robert W Boyd. *Nonlinear optics*. San Diego, CA (United States); Academic Press Inc., 1992.

[57] MD Reid and DF Walls. Quantum theory of nondegenerate four-wave mixing. *Physical Review A*, 34:4929–4955, 1986.

[58] Daniel A Steck. Rubidium 85 d line data (revision 2.1.5), `http://steck.us/alkalidata/rubidium85numbers.pdf`, 2008.

[59] Jürgen Appel, Andrew MacRae, and AI Lvovsky. A versatile digital GHz phase lock for external cavity diode lasers. *Measurement Science and Technology*, 20(5):055302, 2009.

[60] Vincent Boyer, Alberto M Marino, Raphael C Pooser, and Paul D Lett. Entangled images from four-wave mixing. *Science*, 321(5888):544–547, 2008.

[61] D Marcuse. Loss analysis of single-mode fiber splices. *Bell Syst. Tech. J*, 56(5):703–718, 1977.

[62] DN Klyshko. Combine EPR and two-slit experiments: Interference of advanced waves. *Physics Letters A*, 132(6):299–304, 1988.

[63] T Aichele, Alexander I Lvovsky, and S Schiller. Optical mode characterization of single photons prepared by means of conditional measurements on a biphoton state. *The European Physical Journal D-Atomic, Molecular, Optical and Plasma Physics*, 18(2):237–245, 2002.

[64] Pantita Palittapongarnpim, Andrew MacRae, and AI Lvovsky. A monolithic filter cavity for experiments in quantum optics. *Review of Scientific Instruments*, 83(6):066101–066101, 2012.

[65] V Boyer, CF McCormick, E Arimondo, and PD Lett. Ultraslow propagation of matched pulses by four-wave mixing in an atomic vapor. *Physical Review Letters*, 99(14):143601, 2007.

[66] Vivek Venkataraman, Pablo Londero, Amar R Bhagwat, Aaron D Slepkov, and Alexander L Gaeta. All-optical modulation of four-wave mixing in an Rb-filled photonic bandgap fiber. *Optics Letters*, 35(13):2287–2289, 2010.

[67] Andrew MacRae. *An Atomic Source of Quantum Light*. PhD thesis, University of Calgary, 2013.

[68] JS Lundeen, A Feito, H Coldenstrodt-Ronge, KL Pregnell, Ch Silberhorn, TC Ralph, J Eisert, MB Plenio, and IA Walmsley. Tomography of quantum detectors. *Nature Physics*, 5(1):27–30, 2009.

[69] Kristiaan De Greve, Leo Yu, Peter L McMahon, Jason S Pelc, Chandra M Natarajan, Na Young Kim, Eisuke Abe, Sebastian Maier, Christian Schneider, Martin Kamp, et al. Quantum-dot spin-photon entanglement via frequency downconversion to telecom wavelength. *Nature*, 491(7424):421–425, 2012.

[70] Stefan Lund Christensen, JB Béguin, Heidi Lundgaard Sørensen, E Bookjans, D Oblak, JH Müller, J Appel, and ES Polzik. Toward quantum state tomography of a single polariton state of an atomic ensemble. *New Journal of Physics*, 15(1):015002, 2013.

[71] Erwan Bimbard, Rajiv Boddeda, Nicolas Vitrant, Andrey Grankin, Valentina Parigi, Jovica Stanojevic, Alexei Ourjoumtsev, and Philippe Grangier. Homodyne tomography of a single photon retrieved on demand from a cavity-enhanced cold atom memory. *Physical Review Letters*, 112(3):033601, 2014.